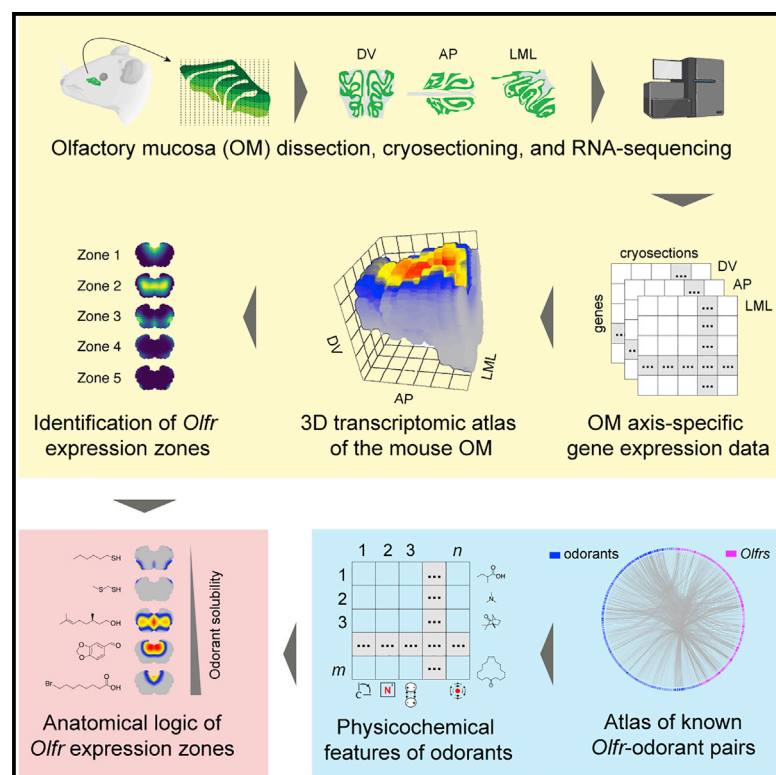


A 3D transcriptomics atlas of the mouse nose sheds light on the anatomical logic of smell

Graphical abstract



Authors

Mayra L. Ruiz Tejada Segura,
Eman Abou Moussa, Elisa Garabello, ...,
Bettina Malnic, Antonio Scialdone,
Luis R. Saraiva

Correspondence

antonio.scialdone@
helmholtz-muenchen.de (A.S.),
saraivalmr@gmail.com (L.R.S.)

In brief

Ruiz Tejada Segura et al. employ a spatial transcriptomics approach to create a 3D map of gene expression of the mouse nose and combine it with single-cell RNA-seq, machine learning, and chemoinformatics to resolve its molecular architecture and shed light into the anatomical logic of smell.

Highlights

- We generate a browsable 3D transcriptomic atlas of the mouse olfactory mucosa (OM)
- We identify potential functional hotspots in the mouse OM
- Odorant receptor genes (*Olf*s) are continuously distributed over at least five zones
- Spatial locations of *Olf*s correlate with the mucus solubility of their ligands



Article

A 3D transcriptomics atlas of the mouse nose sheds light on the anatomical logic of smell

Mayra L. Ruiz Tejada Segura,^{1,2,3,12} Eman Abou Moussa,^{4,12} Elisa Garabello,^{1,5,6} Thiago S. Nakahara,⁷ Melanie Makhoulouf,⁴ Lisa S. Mathew,⁴ Li Wang,⁴ Filippo Valle,⁵ Susie S.Y. Huang,⁴ Joel D. Mainland,^{8,9} Michele Caselle,⁵ Matteo Osella,⁵ Stephan Lorenz,^{4,10} Johannes Reiser,⁸ Darren W. Logan,¹⁰ Bettina Malnic,⁷ Antonio Scialdone,^{1,2,3,13,*} and Luis R. Saraiva^{4,8,11,13,14,*}

¹Institute of Epigenetics and Stem Cells, Helmholtz Zentrum München, Feodor-Lynen-Strasse 21, 81377 München, Germany

²Institute of Functional Epigenetics, Helmholtz Zentrum München, Ingolstädter Landstraße 1, 85764 Neuherberg, Germany

³Institute of Computational Biology, Helmholtz Zentrum München, Ingolstädter Landstraße 1, 85764 Neuherberg, Germany

⁴Sidra Medicine, P.O. Box 26999, Doha, Qatar

⁵Physics Department, University of Turin and INFN, Via P. Giuria 1, 10125 Turin, Italy

⁶Department of Civil and Environmental Engineering, Cornell University, Ithaca, NY 14853, USA

⁷Department of Biochemistry, University of São Paulo, São Paulo, Brazil

⁸Monell Chemical Senses Center, 3500 Market Street, Philadelphia, PA 19104, USA

⁹Department of Neuroscience, University of Pennsylvania, Philadelphia, PA 19104, USA

¹⁰Wellcome Sanger Institute, Wellcome Genome Campus, Hinxton, Cambridge CB10 1SD, UK

¹¹College of Health and Life Sciences, Hamad Bin Khalifa University, P.O. Box 34110, Doha, Qatar

¹²These authors contributed equally

¹³These authors contributed equally

¹⁴Lead contact

*Correspondence: antonio.scialdone@helmholtz-muenchen.de (A.S.), saraivalmr@gmail.com (L.R.S.)

<https://doi.org/10.1016/j.celrep.2022.110547>

SUMMARY

The sense of smell helps us navigate the environment, but its molecular architecture and underlying logic remain understudied. The spatial location of odorant receptor genes (*Olfrs*) in the nose is thought to be independent of the structural diversity of the odorants they detect. Using spatial transcriptomics, we create a genome-wide 3D atlas of the mouse olfactory mucosa (OM). Topographic maps of genes differentially expressed in space reveal that both *Olfrs* and non-*Olfrs* are distributed in a continuous and overlapping fashion over at least five broad zones in the OM. The spatial locations of *Olfrs* correlate with the mucus solubility of the odorants they recognize, providing direct evidence for the chromatographic theory of olfaction. This resource resolves the molecular architecture of the mouse OM and will inform future studies on mechanisms underlying *Olf* gene choice, axonal pathfinding, patterning of the nervous system, and basic logic for the peripheral representation of smell.

INTRODUCTION

The functional logic underlying the topographic organization of primary receptor neurons and their receptive fields is well known for all sensory systems but olfaction (Kandel et al., 2013). The mammalian nose is constantly flooded with odorant cocktails. Powered by a sniff, air enters the nasal cavity until it reaches the olfactory mucosa (OM). There, myriad odorants activate odorant receptors (*Olfrs*) present in the cilia of olfactory sensory neurons (OSNs), triggering a cascade of events that culminate in the brain and result in odor perception (Buck and Axel, 1991; Kandel et al., 2013). Most mouse mature OSNs express a single allele of one out of ~1,100 *Olf* genes (*Olfrs*) (Chess et al., 1994; Hanchate et al., 2015; Malnic et al., 1999; Saraiva et al., 2015b). *Olfrs* employ a combinatorial strategy to detect odorants, which maximizes their detection capacity (Malnic et al., 1999; Nara et al., 2011). OSNs expressing the same *Olf* share similar

odorant response profiles (Malnic et al., 1999; Nara et al., 2011) and drive their axons to the same glomeruli in the olfactory bulb (Mombaerts et al., 1996; Ressler et al., 1994; Vassar et al., 1994). Thus, *Olfrs* define functional units in the olfactory system and function as genetic markers to discriminate between different mature OSN subtypes (Ibarra-Soria et al., 2017; Saraiva et al., 2015b).

Another remarkable feature of the OSN subtypes is their spatial distribution in the OM. Early studies postulated that OSNs expressing different *Olfrs* are spatially segregated into four broad areas within the OM, called “zones,” and which define hemicylindrical rings with different radii (Ressler et al., 1993; Vassar et al., 1993). Subsequent studies identified *Olfrs* expressed across multiple zones, making clear that a division in four discrete zones might not accurately reflect the system, and a continuous numerical index representing the pattern of expression of each *Olf* along the zones was implemented



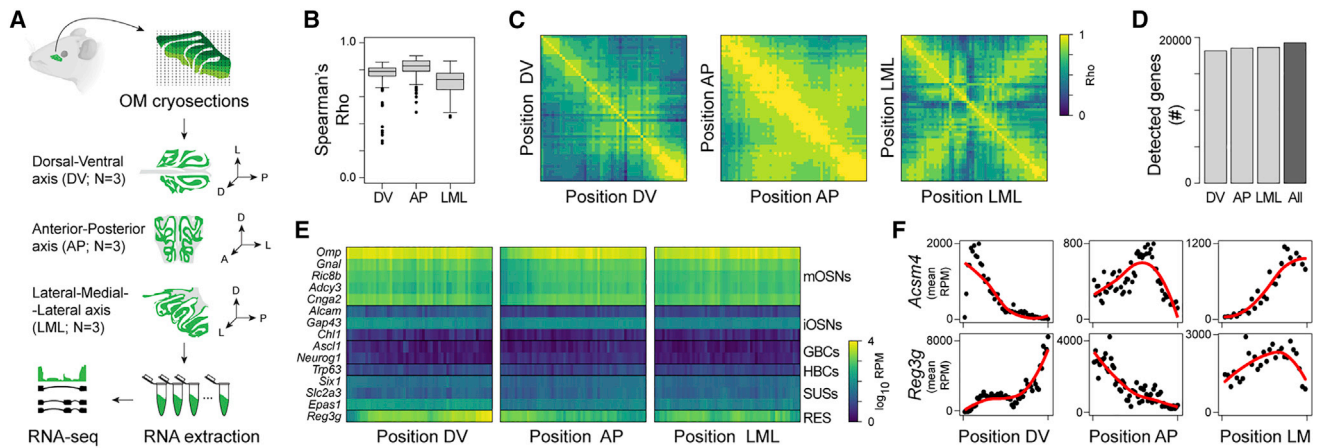


Figure 1. Application of TOMO-seq to mouse OM

(A) Experimental design. TOMO-seq was performed on nine tissue samples, from which three were sliced along the dorsal-ventral axis (DV), three along the anterior-posterior axis (AP), and three along the lateral-medial-lateral axis (LML).

(B) Boxplots showing the distributions of Spearman's correlation coefficients (rho) between replicates in each axis.

(C) Heatmaps showing Spearman's correlation between gene expression patterns at different positions along the three axes.

(D) Number of detected genes along each axis separately or across the whole dataset. Genes were considered as detected when they had at least one normalized count in at least 10% of the samples from one axis.

(E) Heatmaps of log₁₀ normalized expression (after combining the three replicates per axis) of OM canonical markers along the three axes (GBCs, globose basal cells; HBCs, horizontal basal cells; iOSNs, immature olfactory sensory neurons; mOSNs, mature olfactory sensory neurons; RESs, respiratory epithelium cells; RPM, reads per million; SUSs, sustentacular cells).

(F) Normalized expression of canonical OM spatial marker genes along the three axes. Red line shows fits with local polynomial models.

(Miyamichi et al., 2005; Strotmann et al., 1992). More recently, a study reconstructed *Olfr* expression patterns in three dimensions (3D) and qualitatively classified the expression areas of 68 *Olfrs* in nine overlapping zones (Zapiec and Mombaerts, 2020). However, all these studies sampled a fraction (~10%) of the total intact olfactory receptor gene repertoire and, most importantly, lack a quantitative and unbiased definition of zones or indices. We do not currently understand the full complexity of the OM and lack an unbiased and quantitative definition of zones. In effect, the exact number of zones, their anatomical boundaries, molecular identity, and functional relevance are yet to be determined.

One hypothesis is that the topographic distribution of *Olfr* and OSN subtypes evolved because it plays a key role in the process of *Olfr* choice in mature OSNs and/or in OSN axon guidance (Bashkurova et al., 2020; Coppola et al., 2013). An alternative hypothesis is that the spatial organization of *Olfr*/OSN subtypes is tuned to maximize the detection and discrimination of odorants in the peripheral olfactory system (Ressler et al., 1993). Interestingly, the receptive fields of mouse OSNs vary with their spatial location (Ma and Shepherd, 2000), which in some cases correlates with the patterns of odorant sorption in the mouse OM—this association was proposed as the “chromatographic hypothesis” decades before the discovery of the *Olfrs* (Mozell, 1966) and later rebranded as the “sorption hypothesis” in olfaction (Schoenfeld and Cleland, 2006; Scott et al., 2014). While some studies lend support to these hypotheses (reviewed in Secundo et al., 2014), others question their validity (Abaffy and Defazio, 2011; Coppola et al., 2019). Thus, the logic underlying the representation of smell in the peripheral olfactory system still remains unknown, and it is subject of great controversy (Kurian et al., 2021; Secundo et al., 2014).

Spatial transcriptomics, which combines spatial information with high-throughput gene expression profiling, expanded our knowledge of complex tissues, organs, or even entire organisms (Achim et al., 2015; Asp et al., 2019, 2020; Junker et al., 2014; Peng et al., 2016). In this study, we employed a spatial transcriptomics approach to create a 3D map of gene expression of the mouse nose, and we combined it with single-cell RNA sequencing (RNA-seq), machine learning, and chemoinformatics to resolve its molecular architecture and shed light onto the anatomical logic of smell.

RESULTS

A high-resolution spatial transcriptomic map of the mouse olfactory mucosa

We adapted the RNA-seq tomography (Tomo-seq) method (Junker et al., 2014) to create a spatially resolved genome-wide transcriptional atlas of the mouse nose. We obtained cryosections (35 μm) collected along the dorsal-ventral (DV), anterior-posterior (AP), and lateral-medial-lateral (LML) axes (n = 3 per axis) of the OM (Figure 1A) and performed RNA-seq on individual cryosections (see STAR Methods). After quality control (Figures S1A–S1D; Table S1; STAR Methods), we computationally refined the alignment of the cryosection along each axis, and we observed a high correlation between biological replicates (Figure 1B). Hence, we combined the three replicates into a single series of spatial data, including 54, 60, and 56 positions along the DV, AP, and LML axis, respectively (Figure 1C; STAR Methods). On average, we detected >18,000 genes per axis, representing a total of 19,249 genes for all axes combined (Figure 1D). Molecular markers for all canonical cell types known to populate the

mouse OM were detected in all axes (Figure 1E) and expressed at the expected levels (Saraiva et al., 2015b).

Next, we verified the presence of a spatial signal with the Moran's I (Schmal et al., 2017; Figure S1E), whose value is significantly higher than 0 for the data along all axes ($p < 2 \times 10^{-16}$ for all axes), indicating that nearby sections have more similar patterns of gene expression than expected by chance. Given the left/right symmetry along the LML axis (Figure 1C), the data were centered and averaged on the two sides—henceforth, the LML axis will be presented and referred to as the lateral-medial (LM) axis (see STAR Methods). We could reproduce the expression patterns for known OM spatial markers, including the dorso-medial markers *Acsm4* and *Nqo1* (Gussing and Bohm, 2004; Oka et al., 2003) and the ventrolateral markers *Ncam2* and *Reg3g* (Alenius and Bohm, 1997; Yu et al., 2005; Figures 1F and S1F).

Together, these results show that RNA tomography is a sensitive and reliable method to examine gene expression patterns in the mouse OM.

Spatial differential gene expression analysis identifies cell-type-specific expression patterns and functional hotspots in the OM

In the last 3 decades, multiple genes with spatially segregated expression patterns across the OM have been identified. Most of these genes are expressed in mature OSNs and encode chemosensory receptors, transcription factors, adhesion molecules, and many molecules involved in the downstream signaling cascade of receptor activation (Cho et al., 2007; Cloutier et al., 2002; Fulle et al., 1995; Greer et al., 2016; Gussing and Bohm, 2004; Juilfs et al., 1997; Liberles and Buck, 2006; Miyamichi et al., 2005; Norlin et al., 2001; Oka et al., 2003; Pacifico et al., 2012; Saraiva et al., 2015b; Tietjen et al., 2003, 2005; Vassar et al., 1993; Wang et al., 2004; Yoshihara et al., 1997; Yu et al., 2005; Zapiec and Mombaerts, 2020). A smaller number of zonally expressed genes (e.g., metabolizing enzymes, chemokines, and transcription factors) were found to be expressed in sustentacular cells, globose basal cells, olfactory ensheathing cells, Bowman's gland cells, and respiratory epithelial cells (Cloutier et al., 2002; Duggan et al., 2008; Heron et al., 2013; Juilfs et al., 1997; Miyawaki et al., 1996; Norlin et al., 2001; Peluso et al., 2012; Whitby-Logan et al., 2004; Yu et al., 2005). Despite this progress, our knowledge on what genes display true zonal expression patterns and what cell types they are primarily expressed in is still very limited.

To identify axis-specific differentially expressed genes (DEGs) (hereafter referred to as spatial DEGs), we first filtered out lowly expressed genes, then binarized the expression levels at each position according to whether they were higher or lower than their median expression, and applied the Ljung-Box test to the autocorrelation function calculated on the binarized expression values (Figure S2A; STAR Methods). After correcting for multiple testing, we obtained a total of 12,303 spatial DEGs for the three axes combined (false discovery rate [FDR] < 0.01; Figure 2A)—the AP axis showed the highest number of spatial DEGs (10,855), followed by the DV axis (3,658) and the LM (1,318).

Next, we added cell-type resolution to the spatial axes by combining our data with a single-cell RNA-seq (scRNA-seq) dataset from 13 cell types present in the mouse OM (Fletcher et al.,

2017). We cataloged spatial DEGs based on their expression in mature OSNs (mOSNs) versus the 12 other cell types (non-mOSNs; Figures 2B and 2C; Table S2). This led to the identification of 456 spatial DEGs expressed exclusively in non-mOSNs, which are associated with gene ontology (GO) terms, such as transcription factors, norepinephrine metabolism, toxin metabolism, bone development, regulation of cell migration, T cell activation, and others (Table S2). Some genes are expressed across many cell types, but others are specific to one cell type (Figure 2C; Table S2). As expected, some of these genes are cell-specific markers with known spatial expression patterns, such as the sustentacular cells and Bowman's glands markers *Cyp2g1* and *Gstm2* (Yu et al., 2005), the neural progenitor cell markers *Eya2* and *Hes6* (Tietjen et al., 2003), and the basal lamina and olfactory ensheathing cell markers *Aldh1a7* and *Aldh3a1* (Norlin et al., 2001; Table S2). We also identified spatial DEGs along a single axis or multiple axes and specific to one or few cell types (Figures S2B and S2C). For example, the ribosomal protein *Rps21* plays a key role in ribosome biogenesis, cell growth, and death (Wang et al., 2020) and is primarily expressed in horizontal basal cells (HBCs), consistent with their role in the maintenance and regeneration of the OM (Leung et al., 2007). Another example is the extracellular proteinase inhibitor *Wfdc18*, which induces the immune system and apoptosis (Jung et al., 2004) and is expressed in microvillous cells type 1 (MVC1s), consistent with their role in immune responses to viral infection (Baxter et al., 2020). Two more examples are the fibroblast growth factor *Fgf20* in immature sustentacular cells (ISCs) and the adapter protein *Dab2* in mature sustentacular cells (mSCs) (Figures S2B and S2C). *Fgf20* is expressed in several cell types, regulates the horizontal growth of the olfactory turbinates, and is preferentially expressed in the lateral OM (Yang et al., 2018), consistent with our data. *Dab2* regulates mechanisms of tissue formation, modulates immune responses, and participates in the absorption of proteins (Finkielstein and Capeluto, 2016; Park et al., 2019), consistent with the known maintenance and support roles of mSCs in the OM (Brann et al., 2020).

A GO enrichment analysis on the axis-specific DEGs for non-mOSNs genes revealed a very wide variety of biological processes and molecular functions. Some of the notable terms identified were water and fluid transport (e.g., *Ctfr* and *Aqp3*), transcription factors (e.g., *Hes1* and *Dlx5*), oxidation-reduction processes (e.g., *Scd2* and *Cyp2f2*), microtubule cytoskeleton organization involved in mitosis (e.g., *Stil* and *Aurkb*), cell cycle (e.g., *Mcm3* and *Mcm4*), cell division (e.g., *Kif11* and *Cdca3*), negative regulation of apoptosis (e.g., *Dab2* and *Scg2*), sensory perception of chemical stimulus (e.g., *Olfir870* and *Gnas*), and cellular processes (e.g., *Mal* and *Pthlh*), among many others (Table S2).

The identification of thousands of spatial DEGs prompted us to examine their distribution patterns along each axis and the putative functions associated with such spatial clusters of gene expression. We started by using uniform manifold approximation and projection (UMAP) (Becht et al., 2018) and hierarchical clustering to visualize and cluster all spatial DEGs along the three axes. This analysis uncovered nine patterns of expression in the DV and AP axes each and five patterns in the LM axis (Figures 2D and 2E). These patterns include variations of four major

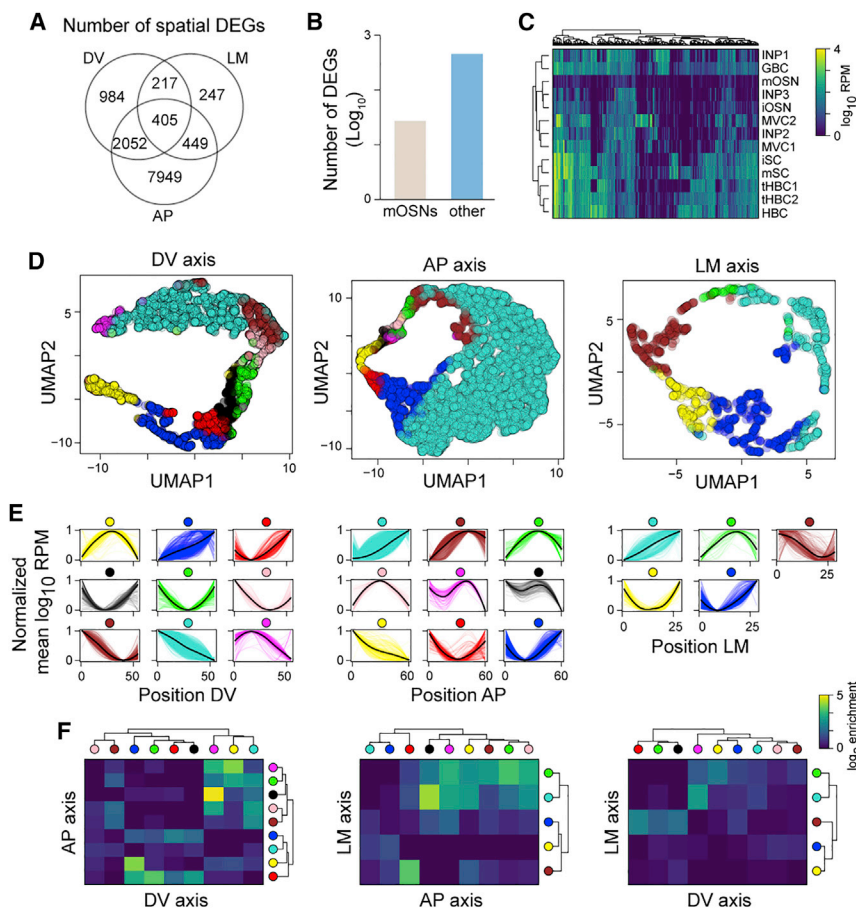


Figure 2. Genes with non-random spatial patterns across different cell types in the OM

(A) Venn diagram showing the numbers of spatial differentially expressed genes (DEGs) along each axis.

(B) Bar plot showing the \log_{10} number of spatial DEGs that are mOSN specific ("mOSNs") or that are detected only in cell types other than mOSNs ("other").

(C) Heatmap of \log_{10} mean expression per cell type of genes that are not expressed in mOSNs but only in other OM cell types (INPs, immediate neuronal precursors; iSCs, immature sustentacular cells; mSCs, mature sustentacular cells; MVCs, microvillous cells; mSCs, mature sustentacular cells).

(D) UMAP plots of spatial DEGs along the three axes ($n = 3$ per axis). Each gene is colored according to the cluster it belongs to.

(E) Normalized average expression patterns of spatial DEGs clusters along the three axes.

(F) Heatmap showing the \log_2 enrichment over the random case for the intersection between lists of genes belonging to different clusters (indicated by colored circles) across pairs of axes.

shapes: monotonically increasing (\nearrow), monotonically decreasing (\searrow), U-shape (\cup), and inverted U-shape (\cap) (Figure 2E). The latter two patterns present clear maximum and minimum at different positions along the axis—for example, the brown, green, pink, magenta, and black AP clusters show a similar inverted U-shape pattern, but their maximum moves along the axis (Figure 2E). As expected, the dorsomedial markers *Acsm4* and *Nqo1* belong to the turquoise clusters in both the DV and LM axes, while the ventrolateral marker *Reg3g* belongs to the blue cluster from the DV axis (Figure 1F; Table S3), mimicking their respective expression pattern in the mouse OM.

The total number of genes per cluster had a median value of 236 but varied greatly between clusters—ranging from 57 in the green LM cluster to 8,551 in the turquoise AP cluster (Figure 2D; Table S3). GO enrichment analyses on the spatial DEGs yielded enriched terms for 14 of the 23 spatial clusters (Table S3). For example, the turquoise AP cluster displaying a monotonically increasing pattern (Figure 2E) yielded GO terms associated with the molecular machinery of mOSNs—such as axonal transportation, RNA processing, ribosomal regulation, and regulation of histone deacetylation (Table S3). Interestingly, the brown DV cluster, which displays a monotonically decreasing expression pattern (Figure 2E), had similar GO term enrichment (Table S3). In agreement with these results, we found that most known OSN activity-

The results above show that OSN activity is enriched in the dorsoposterior region of the OM, which could be due to an enrichment of OSNs in that region. To test this hypothesis, we estimated the abundance and spatial variability of OSNs and five additional major cell types (HBCs, globose basal cells [GBCs], SCs, MVCs, and immediate neuronal precursors [INPs]) in each section through a cell deconvolution analysis (see STAR Methods). We observed statistically significant changes in the abundance of OSNs, which is predicted to be higher in the dorsoposterior region of the OM, as previously suggested (Nickell et al., 2012; Vedin et al., 2009). Conversely, other cell types like HBCs are predicted to have an opposite pattern, as they tend to be more abundant in the anteroventral region (Figure S2F; Table S2).

Next, we extended our GO analysis to the remaining spatial clusters and found additional terms enriched or shared between several clusters among the three axes. For example, GO terms enriched in the dorsomedial region (turquoise DV, pink AP, and LM green clusters) include detoxification of several metabolites and multiple metabolic and catabolic processes, suggesting that this region is involved in the OM detoxification (Table S3). Another example is the enrichment in terms related to the immune system—such as defense response and humoral immune response—in the anteromedial section along the AP axis (yellow, black, and magenta AP and turquoise LM clusters), which

strongly hints at a role of this area in defending OM from pathogenic invaders (Table S3). The anteroventral and posteroventral regions (blue DV and blue AP clusters) are enriched in terms related to the cellular and anatomical organization (e.g., extracellular matrix organization and regulation of cell communication) and bone and cartilage development (e.g., ossification and biomineral tissue development), suggesting these locations are hotspots for the development and regulation of the OM structure. Finally, the ventral portion of the DV (red DV cluster) is associated with terms related to cilia movement and function (e.g., regulation of cilium movement and microtubule-based movement), consistent with both the location and functions of the respiratory epithelium (Yu et al., 2005).

Next, we further explored the relationships between the genes populating each cluster. We found that ventral genes (blue DV cluster) tend to reach a peak in expression in the anterior area of the OM (yellow AP cluster) more often than expected by chance (Figure 2F). We also observed that medial genes (turquoise LM cluster) are more highly expressed in the dorsal (magenta DV cluster) and anterior regions (black, yellow, and magenta AP cluster), while genes peaking in the lateral region (brown LM cluster) tend to be ventral (red DV cluster; Figure 2F). These conclusions hold, even when we exclude *Olfrs* from the analysis (Figure S2D).

These associations between the clusters of spatial DEGs along different axes suggest that the presence of complex 3D expression patterns in OM is not restricted to either *Olfrs* or OSNs. Moreover, our results show that our experimental approach can uncover spatially restricted functional hotspots within the OM.

A 3D transcriptomic atlas of the mouse OM

Since the OR discovery 3 decades ago (Buck and Axel, 1991), *in situ* hybridization (ISH) has been the method of choice to study spatial gene expression patterns across the OM. This method is technically challenging and inherently a very low-throughput experimental approach.

As we showed above, our Tomo-seq data enable a systematic and quantitative estimation of gene expression levels along the three axes of the OM. Here, we take this analysis one step further and generate a fully browsable tridimensional (3D) gene expression atlas of the mouse OM. First, we reconstructed the 3D shape of OM based on publicly available images of OM sections (STAR Methods). We then fed the shape information combined with the gene expression data along the three axes into the iterative proportional fitting (IPF) algorithm (Fienberg, 1970; Junker et al., 2014; Figure 3A). The 3D atlas of the OM faithfully reproduced the known 3D pattern of the dorsomedial marker *Acsn4* (Oka et al., 2003; Figure 3B). To further validate our 3D gene expression atlas of the OM, we compared the 3D reconstructed patterns with conventional ISH patterns for five spatial DEGs identified in this study. The first gene validated was *Cyt11*, which we confirmed to be expressed along the septum throughout the OM (Figures 3C and 3D), consistent with the role *Cyt11* plays in osteogenesis, chondrogenesis, and bone and cartilage homeostasis (Shin et al., 2019; Zhu et al., 2019). The four additional genes (*Olf309*, *Olf618*, *Olf727*, and *Moxd2*) validated via ISH are presented elsewhere in this manuscript (Figures 4, 5, and S4).

To make this 3D gene expression atlas of the mouse OM available to the scientific community, we created a web portal (available at <http://atlas3dnose.helmholtz-muenchen.de:3838/atlas3Dnose>) providing access to the spatial transcriptomic data described here in a browsable and user-friendly format. This portal contains search functionalities allowing the users to perform pattern search by gene, which returns (1) the normalized counts along each of the three axes, (2) the predicted expression pattern in 3D with a zoom function, (3) visualization of the expression patterns in virtual cryosections along the OM by selecting any possible pairwise intersection between two given axes (i.e., DVxAP, DVxLM, and APxLM), (4) the degrees of belonging for each “zone” (see results section below), and (5) single-cell expression data across 14 different cell types.

In sum, here, we generated and made publicly available a highly detailed and fully browsable 3D gene expression atlas of the mouse OM, which allows the exploration of the expression patterns for ~20,000 genes.

Topographical expression patterns of *Olfrs*

In our combined dataset, we detected a total of 959 *Olfrs* (Figure 4A), of which we confidently reconstructed the spatial expression patterns for 689 differentially expressed in space (FDR < 0.01; Figure 4B)—a number six times larger than the combined 112 *Olfrs* characterized by previous ISH studies (Miyamichi et al., 2005; Ressler et al., 1993; Vassar et al., 1994; Zapiec and Mombaerts, 2020). To define *Olf* expression in 3D space in a rigorous, unbiased, and quantitative way, we ran a latent Dirichlet allocation (LDA) algorithm (STAR Methods; Liu et al., 2016) on the 689 spatially differentially expressed *Olfrs*. LDA is a generative statistical model that can infer the topics of a collection of documents based on the variability and frequency of specific words. In the context of this study, if the spatial expression data of *Olfrs* are considered equivalent to “documents,” the inferred topics correspond to “zones” (STAR Methods). We ran LDA for different numbers of zones, and the trend of the log likelihood function suggested that the minimal number of topics required to represent the diversity of patterns is five (Figure S3A; STAR Methods). Next, we visualized the spatial distribution of these five zones in our 3D OM model, with colors representing the probability that a given spatial position belongs to each zone. These five zones extend from the dorsomedial-posterior to the lateroventral-anterior region (Figure 4C), consistent with the previously described zones (Miyamichi et al., 2005; Ressler et al., 1993; Vassar et al., 1993).

The majority of *Olfrs* with known spatial patterns are restricted to a single zone, but a small number of *Olfrs* are expressed across multiple zones in a continuous or non-continuous fashion (Miyamichi et al., 2005; Strotmann et al., 1992; Zapiec and Mombaerts, 2020). Under this logic, each *Olf* has a different probability of belonging to the five topics and zones we identified. To test this assumption, we used the same mathematical framework as above to compute the probabilities that the expression pattern of each *Olf* belongs to a given zone, i.e., the “degree of belonging” (DOB) (Table S4). The DOBs represent a decomposition of the expression patterns in terms of the five zones (Figure 4C) and quantitatively describe the changes in patterns of genes with overlapping areas of expression (e.g., see Figure S3B). The width

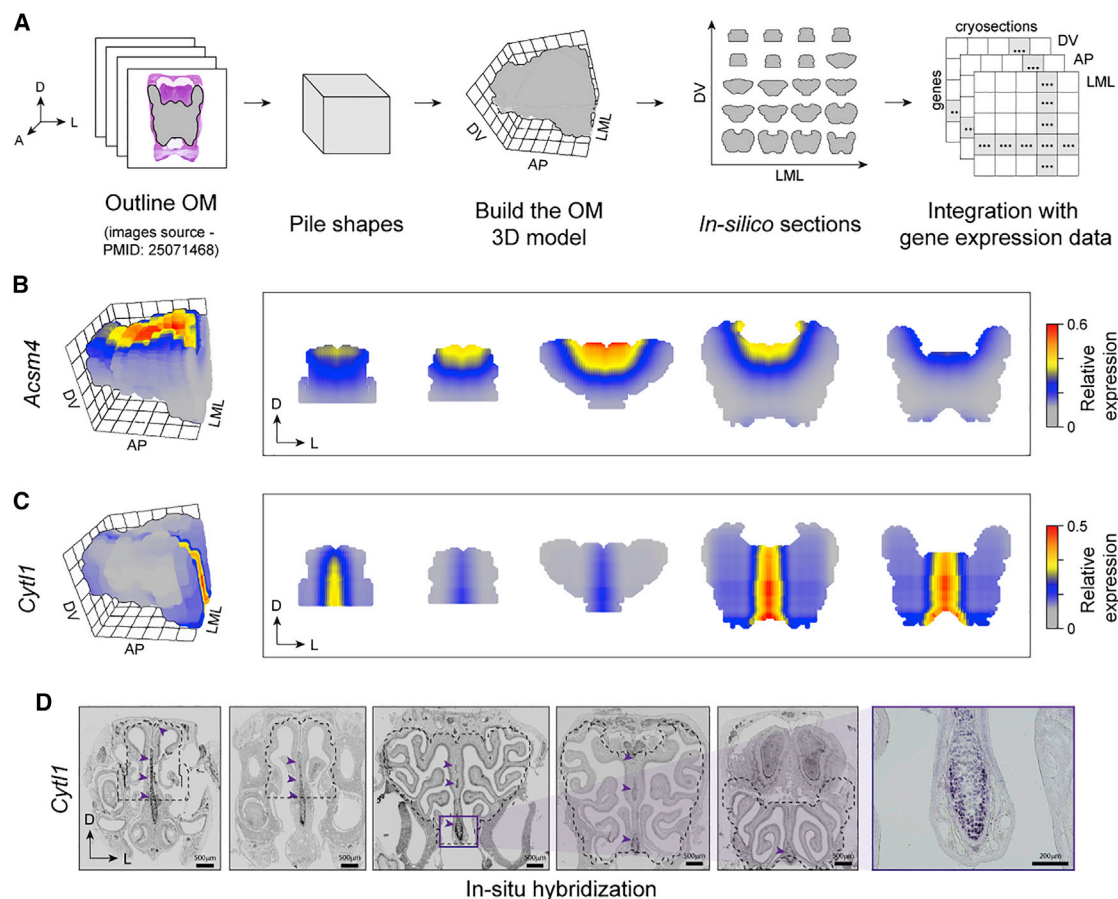


Figure 3. The 3D reconstruction of the OM

(A) Schematic of 3D shape reconstruction strategy. Images of 2D slices along the AP axis of the OM were piled together to build an *in silico* 3D model of OM, which can also be used to visualize *in silico* sections. This 3D model, together with the gene expression data along each axis, was the input of the iterative proportional fitting algorithm, which allowed us to estimate a 3D expression pattern for any gene.

(B and C) Reconstruction of the 3D expression patterns of the *AcsM4* (B) and *Cyt11* (C) in the OM, visualized in 3D and in OM coronal sections taken along the AP axis.

(D) ISH experiment validating *Cyt11* spatial expression pattern reconstructed in (C); note that *Cyt11* is expressed in the septal region all along the OM. Purple arrowheads indicate the location of labeled cells. The dotted outline marks the borders of the OM dissected and used in the RNA-seq experiments and for the construction of the 3D model.

of the distribution of DOBs across the five zones, which can be measured with entropy, can distinguish genes whose patterns mostly fit in a single zone from those spanning multiple zones (Figure S3C; STAR Methods).

To visualize the global distribution of the 689 *Olfrs*, we applied the diffusion map algorithm (Haghverdi et al., 2015) to their DOBs. This showed that the genes are approximately distributed along a continuous line spanning the five zones and without clear borders between zones (Figure 4D), consistent with previous studies (Miyamichi et al., 2005; Strotmann et al., 1992; Zapiec and Mombaerts, 2020). With the diffusion pseudo-time algorithm (Haghverdi et al., 2016), we calculated an index (hereafter referred to as “3D index”) that tracks the position of each *Olfr* gene along the 1D curve in the diffusion map and represents its expression pattern (Figure 4E).

While our approach yielded an index for the 689 spatially differentially expressed *Olfr* genes used to build the diffusion

map, there were 697 *Olfrs* that could not be analyzed, either because they were too lowly expressed or not detected at all in our dataset (Figure 4A). Since the spatial expression patterns for some *Olfrs* are partly associated with their chromosomal and genomic coordinates (Sullivan et al., 1996; Tan and Xie, 2018; Zhang et al., 2004), we hypothesized that we could use a machine-learning algorithm to predict the 3D indices for the 697 *Olfrs* missing from our dataset. Thus, we trained a random forest algorithm on the 3D indices of the spatially differentially expressed *Olfrs* in our dataset using nine genomic features as predictors, such as the chromosomal position, number of *Olfrs* in cluster, and distance to nearest known enhancer (Figure 4F; STAR Methods). The algorithm performance was confirmed by over 100 cross-validation iterations, which revealed a low root-mean-square error ($\leq 10\%$) on the mean 3D index (Figure S4A; STAR Methods). The five most important predictors were features associated with

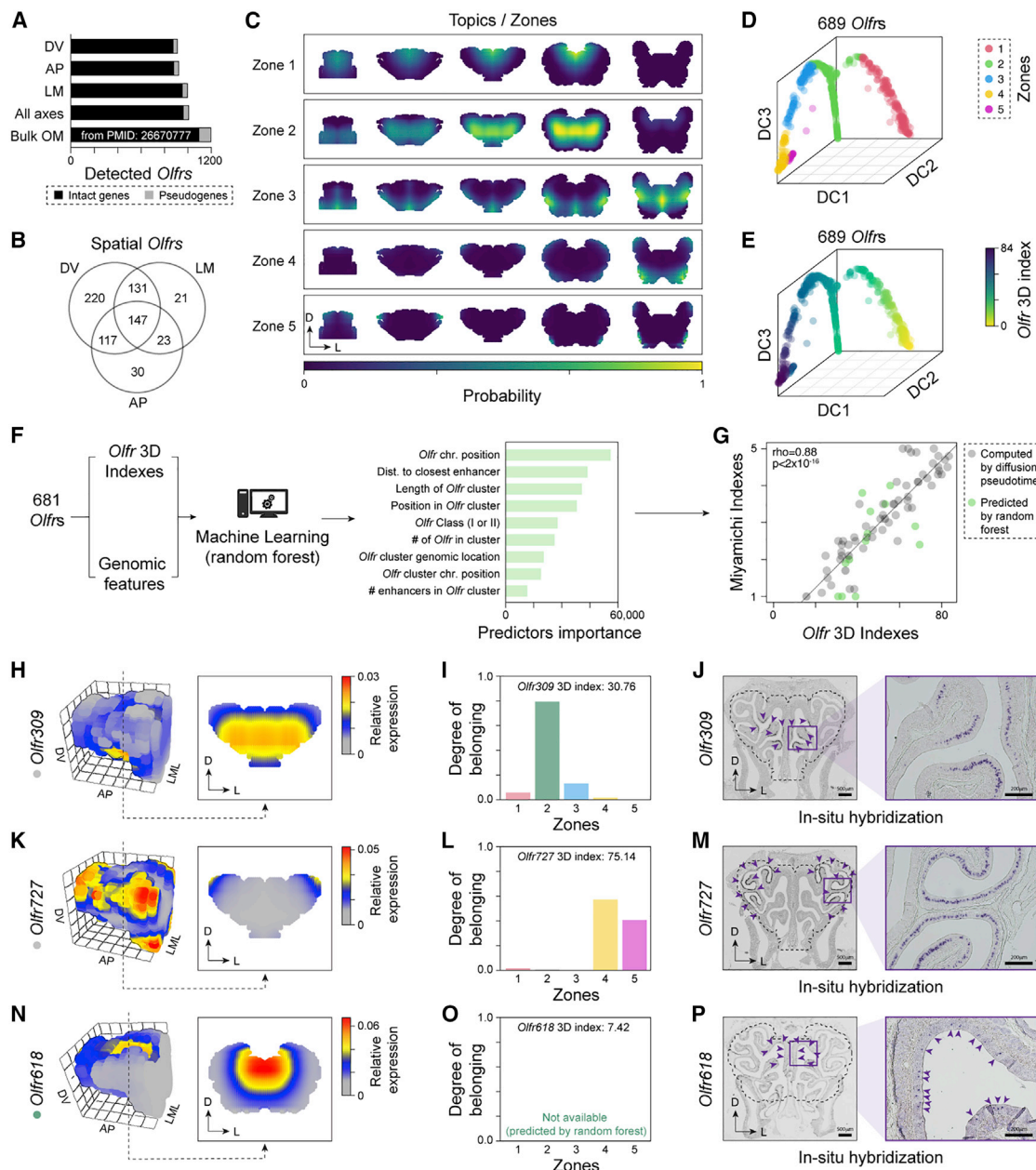


Figure 4. Zonal organization of *Olfrs* in the OM

(A) Number of *Olfrs* detected in our data and in an OM bulk RNA-seq data (Saraiva et al., 2015b).
 (B) Venn diagram of spatially differentially expressed *Olfrs* per axis ($n = 3$ per axis).
 (C) Visualization of the five zones across the OM (coronal sections) estimated with a latent Dirichlet allocation algorithm. The colors indicate the probability (scaled by its maximum value) that a position belongs to a given zone.
 (D) Diffusion map of *Olfrs*. Genes are colored based on the zone they fit in the most. DC, diffusion component.
 (E) Same as (D), with *Olfrs* colored by their 3D index.
 (F) We fitted a random forest algorithm to the 3D indices of 681 spatial *Olfrs* using nine genomic features as predictors. After training, the random forest was used to predict the 3D indices of 697 *Olfrs* that have too low levels in our data.
 (G) 3D indices versus the indices of 80 *Olfrs* estimated in Miyamichi et al. (2005) from ISH data. Black circles indicate *Olfrs* detected in our dataset; green circles are *Olfrs* whose indices were predicted with random forest. The correlation coefficients computed separately on these two sets of *Olfrs* are, respectively, $\rho = 0.92$ ($p < 2 \times 10^{-16}$) and $\rho = 0.69$ ($p = 0.009$).
 (H–P) Predicted expression patterns (H, K, and N), degrees of belonging (I, L, and O), and ISH (J, M, and P) for *Olfr309*, *Olfr727*, and *Olfr618*, respectively. Purple arrowheads indicate the location of labeled cells. The dotted outline marks the borders of the OM dissected and used in the RNA-seq experiments and for the construction of the 3D model.

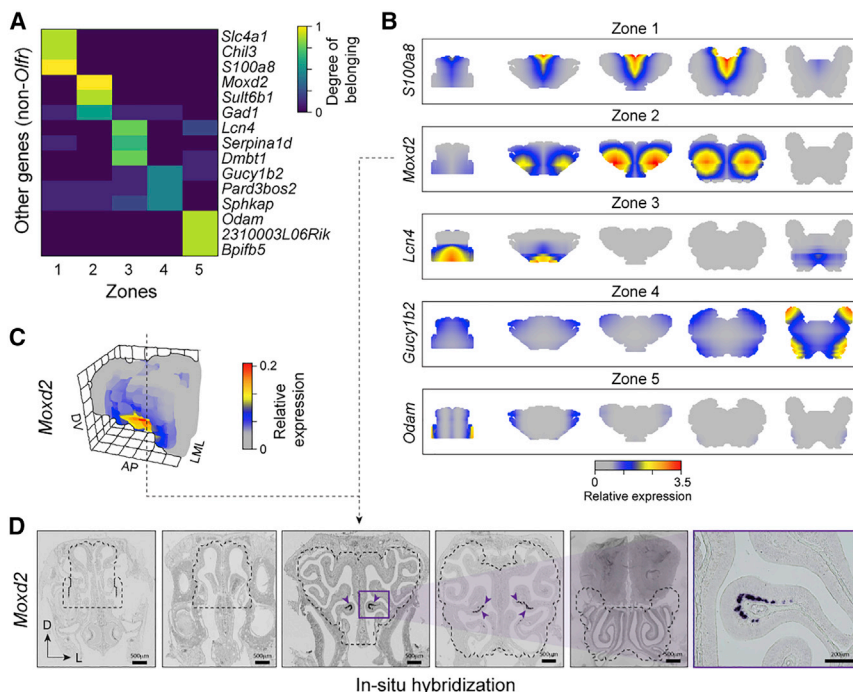


Figure 5. Zonal organization of non-Olfir genes in the OM

(A) Heatmap of degrees of belonging of most zone-specific non-Olfir genes. (B) 3D gene expression pattern (coronal sections) of most topic-specific non-Olfirs for each topic along the AP axis. (C) Reconstruction of the 3D expression pattern of the gene *Moxd2* in the OM. (D) ISH experiment validating *Moxd2* spatial expression pattern reconstructed in (B) and (C). Purple arrowheads indicate the location of ISH-labeled cells. The dotted outline marks the borders of the OM dissected and used in the RNA-seq experiments and for the construction of the 3D model.

Olfir618 (3D index = 7.42; Figures 4H–4P and S4D–S4F; Table S4).

Topographical expression patterns for non-Olfir genes

A recent study performed RNA-seq in 12 randomly dissected OM pieces along the DV axis and identified ~700 non-Olfir genes with putatively spatial patterns (Tan and Xie, 2018), including many genes

chromosomal position, distance to the closest *Olfir* enhancer (Monahan et al., 2017), length of the *Olfir* cluster, position in the *Olfir* cluster, and phylogenetic *Olfir* class (Figure 4F). Using this machine-learning algorithm, we predicted the 3D indices for the 697 *Olfirs* missing reliable expression estimates in our dataset (Table S4).

Overall, through multiple unsupervised and supervised computational methods, we have quantitatively defined five spatial expression domains in the OM (called zones) and have provided accurate 3D spatial indices for 1,386 *Olfirs*, which represents ~98% of the annotated *Olfirs*.

Importantly, we found strong correlations between the “Miyamichi indices” inferred using ISH in Miyamichi et al. (2005) and our 3D indices ($\rho = 0.88$; $p < 2 \times 10^{-16}$; Figure 4G). This correlation remains significant when we separately analyze the 3D indices computed by diffusion pseudo-time ($\rho = 0.92$; $p < 2 \times 10^{-16}$) or predicted by random forest ($\rho = 0.69$; $p = 0.009$). In addition, our indices also correlated with the “Zolfr indices” (Zapiec and Mombaerts, 2020; $\rho = 0.88$; $p < 2 \times 10^{-16}$; Figure S4B), and with the “Tan indices” (Tan and Xie, 2018; $\rho = 0.89$; $p < 2 \times 10^{-16}$; Figure S4C), inferred by ISH and RNA-seq, respectively.

To confirm our predictions, we performed ISH for three *Olfirs* that have not been characterized before—two detected in our dataset and for which the 3D index was calculated via diffusion pseudo-time (DPT) (*Olfir309* and *Olfir727*) and one not detected in our dataset and for which the 3D index was predicted with the random forest algorithm (*Olfir618*). Notably, all three *Olfirs* were expressed primarily within the zones they were predicted to be expressed in: zone 2 for *Olfir309* (3D index = 30.76), zones 4 and 5 for *Olfir727* (3D index = 75.14), and zone 1 for

with zonal expression patterns identified previously (Duggan et al., 2008; Gussing and Bohm, 2004; Liberles and Buck, 2006; Ling et al., 2004; Norlin et al., 2001; Oka et al., 2003; Tietjen et al., 2003; Whitby-Logan et al., 2004; Yoshihara et al., 1997). By identifying 11,538 non-Olfir spatial DEGs (Figures 2 and 3; Table S5), we increased the list of non-Olfir genes with spatial zonation in the OM by 16-fold.

Using the mathematical framework based on topic modeling described above, we decomposed the expression patterns of non-Olfir genes onto the five zones we identified. This allowed us to identify genes showing zone specificity by calculating the entropy of the DOBs distributions. Interestingly, we found 28 genes highly specific for each of the five zones (i.e., with entropy < 1 ; STAR Methods; Figure 5A; Table S5). For example, *S100a8* (zone 1) codes for a calcium-binding protein involved in calcium signaling and inflammation (Yoshikawa et al., 2018), *Moxd2* (zone 2) is a mono-oxygenase dopamine hydroxylase-like protein possibly involved in olfaction (Kim et al., 2014), *Lcn4* (zone 3) is a lipocalin involved in transporting odorants and pheromones (Charkoftaki et al., 2019; Miyawaki et al., 1994), *Gucy1b2* (zone 4) is a soluble guanylyl cyclase oxygen and nitric oxide (Bleymehl et al., 2016; Koglin et al., 2001), and *Odpm* (zone 5) is a secretory calcium-binding phosphoprotein involved in cellular differentiation and matrix protein production and with antimicrobial functions of the junctional epithelium (Lee et al., 2012; Springer et al., 2019; Figure 5B). The high zone specificity of the expression pattern of these genes gives clues into possible biological processes taking place in the zones. Indeed, *Gucy1b2* is a known genetic marker for a small OSN subpopulation localized in cul-de-sac regions in the lateral OM, consistent with our reconstruction (Figure 5B), and it

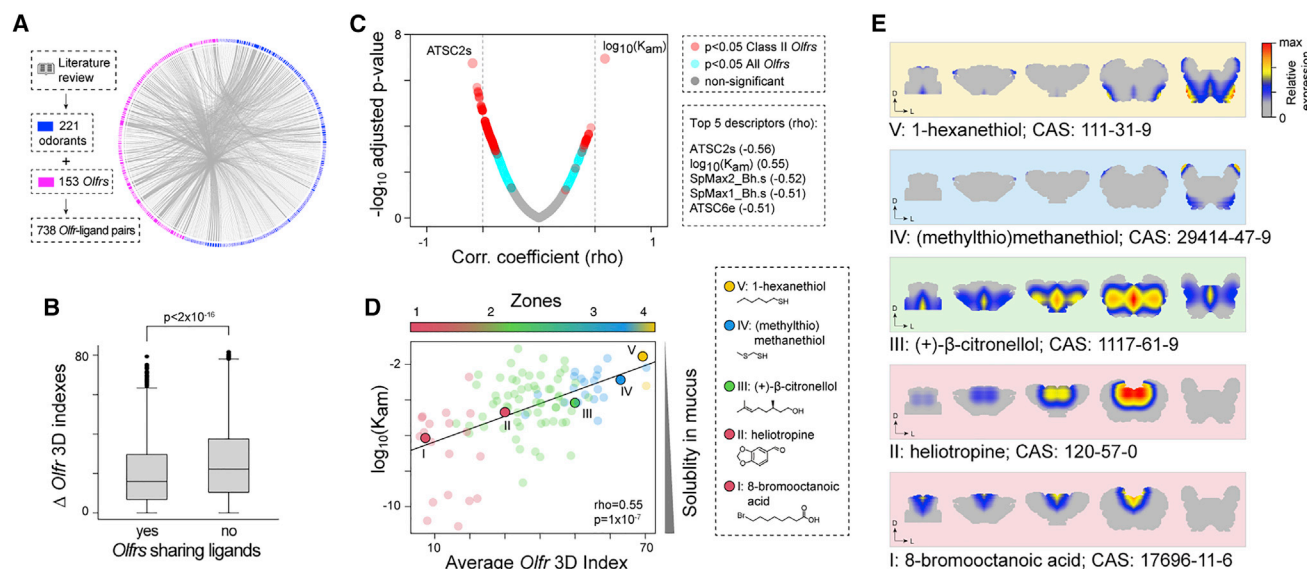


Figure 6. Physiological role of the zones

(A) Circular network illustrating the pairs of Olfrs and ligands that we found in the literature.
(B) Boxplots showing the distributions of the absolute value of 3D index differences between pairs of Olfrs sharing at least one ligand versus pairs of Olfrs without cognate ligands in common. The difference between the two distributions is statistically significant ($p < 2 \times 10^{-16}$; Wilcoxon rank-sum test).
(C) Scatterplot showing the Spearman correlation coefficients between the ligands' mean 3D indices and molecular descriptors and the corresponding $-\log_{10}$ (adjusted p value). Turquoise circles indicate the descriptors having a significant correlation only when both class I and II Olfrs are considered; red circles mark the descriptors with a significant correlation also when class I Olfrs are removed.
(D) Scatterplot illustrating the correlation between air/mucus partition coefficients of the odorants and the average 3D indices of their cognate Olfrs. Only odorants for which we know at least two cognate Olfrs (110) were used here. Odorants are colored according to the zone they belong to (defined as the zone with the highest average degree of belonging computed over all cognate receptors). The five odorants highlighted in the plot by larger circles are indicated on the right-hand side, along with their molecular structure and common name.
(E) Average expression pattern of the cognate Olfrs recognizing each of the five odorants highlighted in (D), including their respective CAS numbers.

regulates the sensing of environmental oxygen levels through the nose (Omura and Mombaerts, 2015; Saraiva et al., 2015b). In addition, our ISH experiments revealed that *Moxd2* is expressed in a small ventrolateral patch of the OM (Figure 5D), validating its predicted 3D spatial pattern (Figures 5B and 5C) and highlighting a potential highly localized role of this protein in neurotransmitter metabolism (Goh et al., 2016) in the mouse OM.

A recent study showed that the transcription factors *Nfia*, *Nfib*, and *Nfix* regulate the zonal expression of Olfrs (Bashkirova et al., 2020). To get some insights into the signaling pathways involved in this process, we mined our dataset for genes encoding ligands and receptors (Efremova et al., 2020) correlated with the expression patterns of the *Nfis* (STAR Methods). This analysis returned 476 genes involved in biological processes associated with the regulation of neurogenesis, regulation of cell development, anatomical structure development, cellular component organization or biogenesis, and regulation of neuron differentiation (Table S5). As expected, some of these genes have known functions in the OM, such as segregating different cell lineages for *Notch1-3* (Carson et al., 2006), genes associated with the development of the nervous system (e.g., *ErbB2* and *Lrp2*; Britsch et al., 1998; Spuch et al., 2012), and many others associated with the semaphorin-plexin, ephrin-Eph, and Slit-Robo signaling complexes—which regulate OSN axon guidance and spatial patterning of the OM (Cloutier et al., 2002; Cutforth et al., 2003; Huber et al., 2003; Kania and Klein, 2016). Excitingly, the majority

of these 476 genes still have unknown functions in the OM, thus highlighting the potential of our approach to discover genes and pathways involved in the regulation of zonal expression in the OM.

The anatomical logic of smell

For most sensory systems, the functional logic underlying the topographic organization of primary receptor neurons and their receptive fields is well known (Kandel et al., 2013). In contrast, the anatomic logic of smell still remains unknown, and it is subject of great controversy and debate (Kurian et al., 2021; Secundo et al., 2014).

To explore the underlying logic linked to the zonal distribution of Olfrs, we investigated possible biases between their expression patterns and the physicochemical properties of their cognate ligands. First, we compiled a list of known 738 Olfr-ligand pairs, representing 153 Olfrs and 221 odorants (Figure 6A; Table S6). Interestingly, Olfr pairs sharing at least one common ligand have more similar expression patterns (i.e., more similar 3D indices) than Olfrs detecting different sets of odorants (Wilcoxon rank-sum test; $p < 2 \times 10^{-16}$; Figure 6B). This observation is consistent with the hypothesis that the Olfr zonal distribution depends, at least partially, on the properties of the odorants they bind to.

Next, we considered a set of 1,210 physicochemical descriptors, including the molecular weight, the number of atoms,

aromaticity index, lipophilicity, and the air/mucus partition coefficient (K_{am}), which quantifies the mucus solubility of each ligand (Rygg et al., 2017; Scott et al., 2014; STAR Methods). We then computed the Spearman's correlation of each of these descriptors of the ligands with the average 3D indices of the Olfrs detecting them. We found a statistically significant correlation for 744 descriptors (FDR < 0.05; Figure 6C; Table S6). The top five highest correlations were with the air/mucus partition coefficient K_{am} ($\rho = 0.55$; adjusted $p = 1 \times 10^{-7}$), ATSC2S ($\rho = -0.56$; adjusted $p = 2 \times 10^{-7}$), SPmax2_Bh.s ($\rho = -0.52$; adjusted $p = 2 \times 10^{-6}$), SPmax1_Bh.s ($\rho = -0.51$; adjusted $p = 3 \times 10^{-6}$), and ATSC6e ($\rho = -0.51$; adjusted $p = 3 \times 10^{-6}$; Figure 6C; Table S6). Interestingly, ATSC2S, SPmax1_Bh.s, and SPmax2_Bh.s are also related to solubility (Consonni and Todeschini, 2008; Devillers and Domine, 1997; Hollas, 2003). Notably, the association between K_{am} and the mean 3D indices does not depend on the number of zones defined with LDA (STAR Methods). Furthermore, it remains robust to changes in the set of ligands and/or Olfrs used for the analysis, namely, when we excluded Olfrs for which the 3D indices were predicted with the random forest model ($\rho = 0.48$; $p = 2 \times 10^{-6}$; Figure S5B) or when only 3D indices from class II Olfrs were included in the analysis ($\rho = 0.5$; $p = 1 \times 10^{-7}$; Figure S5C).

In particular, the positive correlation of the 3D indices with K_{am} (Figure 6D) indicates that the most soluble odorants (lower) preferentially activate Olfrs located in the most antero-dorsomedial region (zone 1) of the OM, while the least soluble odorants (higher K_{am}) activate Olfrs in the postero-ventrolateral region (zones 4 to 5). In other words, gradients of odorants sorption (as defined by their K_{am}) correlate with the gradients of Olfr expression from zone 1 to zone 5, consistent with the chromatographic/sorption hypothesis in olfaction (Mozell, 1966; Scott et al., 2014). This is exemplified by the plots in Figure 6E, illustrating the predicted average expression levels across OM sections of the Olfrs binding to five odorants with different values of K_{am} . These results show a direct association between Olfr spatial patterns and the calculated sorption patterns of their cognate ligands in the OM, providing a potential explanation for the physiological function of the zones in the OM.

DISCUSSION

Past studies yielded inconclusive and sometimes contradictory views on the basic logic underlying the peripheral representation of smell, partly because the topographic distribution of OSN subtypes and their receptive fields still remained vastly uncharted, data on Olfr-ligand pairs were scarce, and there were pitfalls associated with electro-olfactogram recordings used to study spatial patterns of odor recognition in the nose (Kurian et al., 2021; Scott and Scott-Johnson, 2002; Secundo et al., 2015). Here, we combined RNA-seq and computational approaches that utilize unsupervised and supervised machine learning methods to discover and quantitatively characterize spatial expression patterns in the OM. We created a 3D transcriptional map of the mouse OM, which allowed us to spatially characterize 17,628 genes, including ~98% of the annotated Olfrs. We identified and validated by ISH several spatial marker genes, and a clustering analysis pinpointed the OM locations where specific

functions related to, e.g., the immune response might be carried out. We also mathematically defined Olfr expression zones in the OM with an unsupervised machine-learning method based on topic modeling. We estimated that the OM includes at least five zones, which can be used to decompose the expression patterns of all genes. However, our analysis showed that there is a continuous distribution of Olfrs patterns in the OM. Thus, while a discrete number of zones might be convenient to provide a first classification of Olfrs, these might obscure the complexity of the OM spatial patterns. To account for this, we adopted a mathematical framework that can rigorously define zones while capturing finer structures in the data, via the degrees of belonging and the 3D index, which are more suitable to describe Olfrs patterns crossing multiple zones.

The global transcriptomic landscape of the vertebrate OM is similar between individuals and broadly conserved among different vertebrate species, ranging from zebrafish to human (Bear et al., 2016; Saraiva et al., 2015a, 2019). Similarly, the spatial segregation of Olfrs into partially overlapping rings of expression, centered around the midline structure of the OM, is also conserved among vertebrates (Freitag et al., 1995; Horowitz et al., 2014; Marchand et al., 2004; Miyamichi et al., 2005; Octura et al., 2018; Ressler et al., 1993; Strotmann et al., 1992; Vassar et al., 1993; Weth et al., 1996). While the number of Olfr zones in zebrafish, frog, and salamander still remain unknown (Freitag et al., 1995; Marchand et al., 2004; Weth et al., 1996), ISH studies suggested that the total number of Olfr expression zones can vary between mammals—ranging from two in macaque (Horowitz et al., 2014) to four in rat (Vassar et al., 1993) and goat (Octura et al., 2018), and between four and nine in mouse (Miyamichi et al., 2005; Ressler et al., 1993; Zapiec and Mombaerts, 2020). While the exact number of Olfr expression zones in OM still remains under debate, our results are consistent with both another recent RNA-seq study (Tan and Xie, 2018) and the largest Olfr ISH study in the mouse OM (Miyamichi et al., 2005), thus supporting the existence of at least five overlapping Olfr expression zones in the mouse nose.

Taking into account how conserved the molecular organization of the OM is in vertebrates, the 2-fold reduction in the number of Olfr expression zones in macaque compared with rodents and goat (an ungulate) is puzzling. While we cannot exclude the presence of confounding factors (e.g., limited Olfr sampling and/or inconsistent definitions of “zones”), it is interesting that the 2-fold reduction in number of zones is associated with a 2-fold reduction in the number of annotated intact Olfrs in macaque (and other higher primates, including human) compared with other rodents and ungulates (Horowitz et al., 2014; Niimura et al., 2014; Saraiva et al., 2019). Since the accelerated loss of Olfr genes during primate evolution has been linked to the acquisition of trichromatic acute vision and dietary changes (Niimura et al., 2018), it is plausible that these evolutionary pressures also helped shape the spatial distribution of Olfrs in macaques and other primates, including human.

The quantitative framework we built for this dataset will facilitate the interrogation of gene expression patterns via an online tool we provide and help answer important questions on the physiology of the nose. Our approach could be easily applied to spatial transcriptomic data collected from other tissues to

perform comparisons across tissues from different species or the same tissue across multiple developmental stages. Moreover, the results from this study serve as a template to start answering other important questions about olfaction, such as whether *Olf* spatial expression maps can encode maps of odor perception. Because the general molecular mechanisms of olfaction, zonal organization of *Olf*s, conservation of ligands among *Olf* orthologs, and components of olfactory perception are conserved in mammals (Adipietro et al., 2012; Bear et al., 2016; Freitag et al., 1995; Horowitz et al., 2014; Kurian et al., 2021; Manoel et al., 2021; Octura et al., 2018; Saraiva et al., 2019; Weth et al., 1996), the association we uncovered here between *Olf* zones and the solubility of odorants they detect can likely be extrapolated to other mammals, including humans. Finally, the functional logic underlying the mammalian topographic organization of primary receptor neurons and their receptive fields in smell is now starting to be exposed.

Limitations of the study

This study enabled us to answer fundamental and long-standing questions about the rationale behind the spatial organization of the peripheral olfactory system. Specifically, we provide evidence to the hypothesis that the spatial zones increase the discriminatory power of the olfactory system by distributing *Olf*s in the areas of the OM more likely to be reached by their cognate ligands, based on their solubility in mucus. A caveat of this approach is that the *Olf*-ligand list we compiled from the literature includes odorant libraries of different size and composition and tested using different experimental approaches. Moreover, highly abundant *Olf*s have a higher probability of being deorphanized than lowly abundant *Olf*s, and ecologically relevant odorants are more likely to activate *Olf*s when compared with other odorants (Dunkel et al., 2014; Saraiva et al., 2019; Trimmer and Mainland, 2017). Despite having compiled and performed our analysis on the largest set of *Olf*-ligand pairs assembled to date and carrying out multiple robustness checks, we cannot rule out that ascertainment bias might contribute to the associations we found between the *Olf* spatial location and the properties of their respective ligands. Future studies investigating the activation profiles for all mouse *Olf*s and/or mapping the *in vivo* activation patterns of mouse *Olf*s in the olfactory mucosa will be key to stress test the conclusions of our study.

STAR★METHODS

Detailed methods are provided in the online version of this paper and include the following:

- KEY RESOURCES TABLE
- RESOURCE AVAILABILITY
 - Lead contact
 - Materials availability
 - Data and code availability
- EXPERIMENTAL MODEL AND SUBJECT DETAILS
 - Animals
- METHOD DETAILS
 - Dissection of the olfactory mucosa, cryosections, and RNA-sequencing

- RNA-seq data mapping and gene counting
- Quality control
- Data normalization
- Identification of differentially expressed genes and gene clustering
- Combining Tomo-seq with single-cell RNA-seq data
- Gene ontology (GO) enrichment analysis
- Cell type deconvolution analysis
- Identification of ligands and receptors associated with the NfiA, NfiB or NfiX transcription factors
- 3D spatial reconstruction
- Definition of zones by topic modelling
- Definition of *Olf* 3D indexes via diffusion pseudo-time
- Prediction of zone index for undetected *Olf*s with Random Forest
- Odorant information and *Olf*-ligand pairs
- Correlation analysis of physico-chemical descriptors with 3D index
- *In-situ* hybridization

● QUANTIFICATION AND STATISTICAL ANALYSIS

SUPPLEMENTAL INFORMATION

Supplemental information can be found online at <https://doi.org/10.1016/j.celrep.2022.110547>.

ACKNOWLEDGMENTS

We would like to thank Ximena Ibarra-Soria for help with the initial analysis and Maria-Elena Torres-Padilla, Bob Datta, Giorgia Greco, and the members of the Saraiva and Scialdone Labs for the constructive feedback, insightful discussions, and helpful comments. This work was supported by the Helmholtz Association (A.S.), the Deutsche Forschungsgemeinschaft (SC280/2–1 to A.S.), the National Institutes of Health (R01DC016647 to J.R.), and Sidra Medicine (SDR400040 to L.R.S.)—a member of Qatar Foundation.

AUTHOR CONTRIBUTIONS

M.L.R.T.S. analyzed data and wrote the initial version of the manuscript. E.A.M. performed the RNA-seq experiments and analyzed data. T.S.N., L.S.M., L.W., and S.L. performed experiments. M.M., S.S.Y.H., J.D.M., F.V., M.C., and M.O. analyzed data. E.G., J.R., D.W.L., and B.M. analyzed data and helped write the manuscript. A.S. and L.R.S. conceived and supervised the project, analyzed data, and wrote the final version of the manuscript.

DECLARATION OF INTERESTS

The authors declare no competing interests.

Received: September 13, 2021

Revised: January 26, 2022

Accepted: March 1, 2022

Published: March 22, 2022

REFERENCES

- Abaify, T., and Defazio, A.R. (2011). The location of olfactory receptors within olfactory epithelium is independent of odorant volatility and solubility. *BMC Res. Notes* 4, 137.
- Abaify, T., Matsunami, H., and Luetje, C.W. (2006). Functional analysis of a mammalian odorant receptor subfamily. *J. Neurochem.* 97, 1506–1518.

- Achim, K., Pettit, J.-B., Saraiva, L.R., Gavriouchkina, D., Larsson, T., Arendt, D., and Marioni, J.C. (2015). High-throughput spatial mapping of single-cell RNA-seq data to tissue of origin. *Nat. Biotechnol.* **33**, 503–509.
- Adipietro, K.A., Mainland, J.D., and Matsunami, H. (2012). Functional evolution of mammalian odorant receptors. *PLoS Genet.* **8**, e1002821.
- Aldinucci, M., Bagnasco, S., Lusso, S., Pasteris, P., Rabellino, S., and Vallero, S. (2017). OCCAM: a flexible, multi-purpose and extendable HPC cluster. *J. Phys. Conf. Ser.* **898**, 082039.
- Alenius, M., and Bohm, S. (1997). Identification of a novel neural cell adhesion molecule-related gene with a potential role in selective axonal projection. *J. Biol. Chem.* **272**, 26083–26086.
- Allee, H., and Theis, F.J. (2021). AutoGeneS: automatic gene selection using multi-objective optimization for RNA-seq deconvolution. *Cell Syst.* **12**, 706–715.e4.
- Anders, S., Pyl, P.T., and Huber, W. (2014). HTSeq - a Python framework to work with high-throughput sequencing data. *Bioinformatics* **31**, 166–169.
- Angerer, P., Haghverdi, L., Buttner, M., Theis, F.J., Marr, C., and Buettner, F. (2016). destiny: diffusion maps for large-scale single-cell data in R. *Bioinformatics* **32**, 1241–1243.
- Araneda, R.C., Peterlin, Z., Zhang, X., Chesler, A., and Firestein, S. (2004). A pharmacological profile of the aldehyde receptor repertoire in rat olfactory epithelium. *J. Physiol.* **555**, 743–756.
- Asp, M., Giacomello, S., Larsson, L., Wu, C., Furth, D., Qian, X., Wardell, E., Custodio, J., Reimegard, J., Salmen, F., et al. (2019). A spatiotemporal organ-wide gene expression and cell atlas of the developing human heart. *Cell* **179**, 1647–1660.e19.
- Asp, M., Bergenstrahle, J., and Lundberg, J. (2020). Spatially resolved transcriptomes-next generation tools for tissue exploration. *Bioessays* **42**, e1900221.
- Barrios, A.W., Nunez, G., Sanchez Quinteiro, P., and Salazar, I. (2014). Anatomy, histochemistry, and immunohistochemistry of the olfactory subsystems in mice. *Front. Neuroanat.* **8**, 63.
- Bashkirova, E., Monahan, K., Campbell, C.E., Osinski, J.M., Tan, L., Schieren, I., Barnea, G., Xie, X.S., Gronostajski, R.M., and Lomvardas, S. (2020). Homeotic regulation of olfactory receptor choice via NF1-dependent heterochromatic silencing and genomic compartmentalization. Preprint at bioRxiv. <https://doi.org/10.1101/2020.08.30.274035>.
- Baxter, B.D., Larson, E.D., Merle, L., Feinstein, P., Polese, A.G., Bubak, A.N., Niemeyer, C.S., Hassell, J., Shepherd, D., Ramakrishnan, V.R., et al. (2020). Transcriptional profiling reveals potential involvement of microvillous TRPM5-expressing cells in viral infection of the olfactory epithelium. Preprint at bioRxiv. <https://doi.org/10.1101/2020.05.14.096016>.
- Bear, D.M., Lassance, J.-M., Hoekstra, H.E., and Datta, S.R. (2016). The evolving neural and genetic architecture of vertebrate olfaction. *Curr. Biol.* **26**, R1039–R1049.
- Becht, E., McInnes, L., Healy, J., Dutertre, C.A., Kwok, I.W.H., Ng, L.G., Ginhoux, F., and Newell, E.W. (2018). Dimensionality reduction for visualizing single-cell data using UMAP. *Nat. Biotechnol.* **37**, 38–44.
- Blei, D.M., Ng, A.Y., and Jordan, M.I. (2003). Latent dirichlet allocation. *J. Mach. Learn. Res.* **3**, 993–1022.
- Bleymehl, K., Perez-Gomez, A., Omura, M., Moreno-Perez, A., Macias, D., Bai, Z., Johnson, R.S., Leinders-Zufall, T., Zufall, F., and Mombaerts, P. (2016). A sensor for low environmental oxygen in the mouse main olfactory epithelium. *Neuron* **92**, 1196–1203.
- Bozza, T., Feinstein, P., Zheng, C., and Mombaerts, P. (2002). Odorant receptor expression defines functional units in the mouse olfactory system. *J. Neurosci.* **22**, 3033–3043.
- Brann, D.H., Tsukahara, T., Weinreb, B., Lipovsek, M., Van den Berge, K., Gong, B., Chance, R., Macaulay, I.C., Chou, H.J., Fletcher, R.B., et al. (2020). Non-neuronal expression of SARS-CoV-2 entry genes in the olfactory system suggests mechanisms underlying COVID-19-associated anosmia. *Sci. Adv.* **6**, eabc5801.
- Britsch, S., Li, L., Kirchhoff, S., Theuring, F., Brinkmann, V., Birchmeier, C., and Riethmacher, D. (1998). The ErbB2 and ErbB3 receptors and their ligand, neu-regulin-1, are essential for development of the sympathetic nervous system. *Genes Dev.* **12**, 1825–1836.
- Buck, L., and Axel, R. (1991). A novel multigene family may encode odorant receptors: a molecular basis for odor recognition. *Cell* **65**, 175–187.
- Carson, C., Murdoch, B., and Roskams, A.J. (2006). Notch 2 and Notch 1/3 segregate to neuronal and glial lineages of the developing olfactory epithelium. *Dev. Dyn.* **235**, 1678–1688.
- Charkoftaki, G., Wang, Y., McAndrews, M., Bruford, E.A., Thompson, D.C., Vasiliou, V., and Nebert, D.W. (2019). Update on the human and mouse lipocalin (LCN) gene family, including evidence the mouse Mup cluster is result of an “evolutionary bloom”. *Hum. Genomics* **13**, 11.
- Chess, A., Simon, I., Cedar, H., and Axel, R. (1994). Allelic inactivation regulates olfactory receptor gene expression. *Cell* **78**, 823–834.
- Cho, J.H., Lepine, M., Andrews, W., Parnavelas, J., and Cloutier, J.F. (2007). Requirement for Slit-1 and Robo-2 in zonal segregation of olfactory sensory neuron axons in the main olfactory bulb. *J. Neurosci.* **27**, 9094–9104.
- Cloutier, J.F., Giger, R.J., Koentges, G., Dulac, C., Kolodkin, A.L., and Ginty, D.D. (2002). Neuropilin-2 mediates axonal fasciculation, zonal segregation, but not axonal convergence, of primary accessory olfactory neurons. *Neuron* **33**, 877–892.
- Consonni, and Todeschini, R. (2008). New spectral indices for molecule description. *MATCH Commun. Math. Comput. Sci.* **60**, 3–14.
- Coppola, D.M., Fitzwater, E., Rygg, A.D., and Craven, B.A. (2019). Tests of the chromatographic theory of olfaction with highly soluble odors: a combined electro-olfactogram and computational fluid dynamics study in the mouse. *Biol. Open* **8**, bio047217.
- Coppola, D.M., Waggner, C.T., Radwani, S.M., and Brooks, D.A. (2013). An electroolfactogram study of odor response patterns from the mouse olfactory epithelium with reference to receptor zones and odor sorptiveness. *J. Neurophysiol.* **109**, 2179–2191.
- Cutforth, T., Moring, L., Mendelsohn, M., Nemes, A., Shah, N.M., Kim, M.M., Frisen, J., and Axel, R. (2003). Axonal ephrin-As and odorant receptors: coordinate determination of the olfactory sensory map. *Cell* **114**, 311–322.
- Devillers, J., and Domine, D. (1997). Comparison of reliability of log P values calculated from a group contribution approach and from the autocorrelation method. *SAR QSAR Environ. Res.* **7**, 195–232.
- Dey, K.K., Hsiao, C.J., and Stephens, M. (2017). Visualizing the structure of RNA-seq expression data using grade of membership models. *PLoS Genet.* **13**, e1006599.
- Dobin, A., Davis, C.A., Schlesinger, F., Drenkow, J., Zaleski, C., Jha, S., Batut, P., Chaisson, M., and Gingeras, T.R. (2013). STAR: ultrafast universal RNA-seq aligner. *Bioinformatics* **29**, 15–21.
- Duggan, C.D., DeMaria, S., Baudhuin, A., Stafford, D., and Ngai, J. (2008). Foxg1 is required for development of the vertebrate olfactory system. *J. Neurosci.* **28**, 5229–5239.
- Dunkel, A., Steinhaus, M., Kotthoff, M., Nowak, B., Krautwurst, D., Schieberle, P., and Hofmann, T. (2014). Nature’s chemical signatures in human olfaction: a foodborne perspective for future biotechnology. *Angew. Chem. Int. Ed. Engl.* **53**, 7124–7143.
- Efremova, M., Vento-Tormo, M., Teichmann, S.A., and Vento-Tormo, R. (2020). CellPhoneDB: inferring cell-cell communication from combined expression of multi-subunit ligand-receptor complexes. *Nat. Protoc.* **15**, 1484–1506.
- Fienberg, S.E. (1970). An iterative procedure for estimation in contingency tables. *Ann. Math. Stat.* **41**, 907–917.
- Finkelstein, C.V., and Capelluto, D.G. (2016). Disabled-2: a modular scaffold protein with multifaceted functions in signaling. *Bioessays* **38**, S45–S55.
- Fletcher, R.B., Das, D., Gadye, L., Street, K.N., Baudhuin, A., Wagner, A., Cole, M.B., Flores, Q., Choi, Y.G., Yosef, N., et al. (2017). Deconstructing olfactory stem cell trajectories at single-cell resolution. *Cell Stem Cell* **20**, 817–830.e8.

- Floriano, W.B., Vaidehi, N., Goddard, W.A., 3rd, Singer, M.S., and Shepherd, G.M. (2000). Molecular mechanisms underlying differential odor responses of a mouse olfactory receptor. *Proc. Natl. Acad. Sci. U S A* 97, 10712–10716.
- Freitag, J., Krieger, J., Strotmann, J., and Breer, H. (1995). Two classes of olfactory receptors in *Xenopus laevis*. *Neuron* 15, 1383–1392.
- Fulle, H.J., Vassar, R., Foster, D.C., Yang, R.B., Axel, R., and Garbers, D.L. (1995). A receptor guanylyl cyclase expressed specifically in olfactory sensory neurons. *Proc. Natl. Acad. Sci. U S A* 92, 3571–3575.
- Gaillard, I., Rouquier, S., Pin, J.P., Mollard, P., Richard, S., Barnabe, C., Demaille, J., and Giorgi, D. (2002). A single olfactory receptor specifically binds a set of odorant molecules. *Eur. J. Neurosci.* 15, 409–418.
- Godfrey, P.A., Malnic, B., and Buck, L.B. (2004). The mouse olfactory receptor gene family. *Proc. Natl. Acad. Sci. U S A* 101, 2156–2161.
- Goh, C.-J., Choi, D., Park, D.B., Kim, H., and Hahn, Y. (2016). MOXD2, a gene possibly associated with olfaction, is frequently inactivated in birds. *PLoS One* 11, e0152431.
- Greer, P.L., Bear, D.M., Lassance, J.M., Bloom, M.L., Tsukahara, T., Pashkovski, S.L., Masuda, F.K., Nowlan, A.C., Kirchner, R., Hoekstra, H.E., et al. (2016). A Family of non-GPCR chemosensors defines an alternative logic for mammalian olfaction. *Cell* 165, 1734–1748.
- Grosmaître, X., Vassalli, A., Mombaerts, P., Shepherd, G.M., and Ma, M. (2006). Odorant responses of olfactory sensory neurons expressing the odorant receptor MOR23: a patch clamp analysis in gene-targeted mice. *Proc. Natl. Acad. Sci. U S A* 103, 1970–1975.
- Grosmaître, X., Fuss, S.H., Lee, A.C., Adipietro, K.A., Matsunami, H., Mombaerts, P., and Ma, M. (2009). SR1, a mouse odorant receptor with an unusually broad response profile. *J. Neurosci.* 29, 14545–14552.
- Gussing, F., and Böhm, S. (2004). NQO1 activity in the main and the accessory olfactory systems correlates with the zonal topography of projection maps. *Eur. J. Neurosci.* 19, 2511–2518.
- Haghverdi, L., Büttner, F., and Theis, F.J. (2015). Diffusion maps for high-dimensional single-cell analysis of differentiation data. *Bioinformatics* 31, 2989–2998.
- Haghverdi, L., Büttner, M., Wolf, F.A., Büttner, F., and Theis, F.J. (2016). Diffusion pseudotime robustly reconstructs lineage branching. *Nat. Methods* 13, 845–848.
- Hanchate, N.K., Kondoh, K., Lu, Z., Kuang, D., Ye, X., Qiu, X., Pachter, L., Trapnell, C., and Buck, L.B. (2015). Single-cell transcriptomics reveals receptor transformations during olfactory neurogenesis. *Science* 350, 1251–1255.
- Heron, P.M., Stromberg, A.J., Breheny, P., and McClintock, T.S. (2013). Molecular events in the cell types of the olfactory epithelium during adult neurogenesis. *Mol. Brain* 6, 49.
- Hollas, B. (2003). An analysis of the autocorrelation descriptor for molecules. *J. Math. Chem.* 33, 91–101.
- Horowitz, L.F., Saraiva, L.R., Kuang, D., Yoon, K.H., and Buck, L.B. (2014). Olfactory receptor patterning in a higher primate. *J. Neurosci.* 34, 12241–12252.
- Huber, A.B., Kolodkin, A.L., Ginty, D.D., and Cloutier, J.F. (2003). Signaling at the growth cone: ligand-receptor complexes and the control of axon growth and guidance. *Annu. Rev. Neurosci.* 26, 509–563.
- Ibarra-Soria, X., Nakahara, T.S., Lilue, J., Jiang, Y., Trimmer, C., Souza, M.A., Netto, P.H., Ikegami, K., Murphy, N.R., Kusma, M., et al. (2017). Variation in olfactory neuron repertoires is genetically controlled and environmentally modulated. *Elife* 6, e21476.
- Jiang, Y., Gong, N.N., Hu, X.S., Ni, M.J., Pasi, R., and Matsunami, H. (2015). Molecular profiling of activated olfactory neurons identifies odorant receptors for odors *in vivo*. *Nat. Neurosci.* 18, 1446–1454.
- Jones, E.M., Jajoo, R., Cancilla, D., Lubock, N.B., Wang, J., Satyadi, M., Cheung, R., de March, C., Bloom, J.S., Matsunami, H., et al. (2019). A scalable, multiplexed assay for decoding GPCR-ligand interactions with RNA sequencing. *Cell Syst.* 8, 254–260.e6.
- Juif, D.M., Fulle, H.J., Zhao, A.Z., Houslay, M.D., Garbers, D.L., and Beavo, J.A. (1997). A subset of olfactory neurons that selectively express cGMP-stimulated phosphodiesterase (PDE2) and guanylyl cyclase-D define a unique olfactory signal transduction pathway. *Proc. Natl. Acad. Sci. U S A* 94, 3388–3395.
- Jung, D.J., Bong, J.J., and Baik, M. (2004). Extracellular proteinase inhibitor-accelerated apoptosis is associated with B cell activating factor in mammary epithelial cells. *Exp. Cell Res.* 292, 115–122.
- Junker, J.P., Noel, E.S., Guryev, V., Peterson, K.A., Shah, G., Huiskens, J., McMahon, A.P., Berezikov, E., Bakkers, J., and van Oudenaarden, A. (2014). Genome-wide RNA tomography in the zebrafish embryo. *Cell* 159, 662–675.
- Kajiya, K., Inaki, K., Tanaka, M., Haga, T., Kataoka, H., and Touhara, K. (2001). Molecular bases of odor discrimination: reconstitution of olfactory receptors that recognize overlapping sets of odorants. *J. Neurosci.* 21, 6018–6025.
- Kandel, E., Schwartz, J., Jessell, T., Siegelbaum, S., and Hudspeth, A. (2013). *In Principles of Neural Science*, Fifth edition (McGraw-Hill).
- Kania, A., and Klein, R. (2016). Mechanisms of ephrin-Eph signalling in development, physiology and disease. *Nat. Rev. Mol. Cell. Biol.* 17, 240–256.
- Kim, D.S., Wang, Y., Oh, H.J., Lee, K., and Hahn, Y. (2014). Frequent loss and alteration of the MOXD2 gene in catarrhines and whales: a possible connection with the evolution of olfaction. *PLoS One* 9, e104085.
- Kinsella, R.J., Kahari, A., Haider, S., Zamora, J., Proctor, G., Spudich, G., Almeida-King, J., Staines, D., Derwent, P., Kerhornou, A., et al. (2011). Ensembl BioMarts: a hub for data retrieval across taxonomic space. *Database* 2011, bar030.
- Koglin, M., Vehse, K., Budaus, L., Scholz, H., and Behrends, S. (2001). Nitric oxide activates the beta 2 subunit of soluble guanylyl cyclase in the absence of a second subunit. *J. Biol. Chem.* 276, 30737–30743.
- Kurian, S.M., Naressi, R.G., Manoel, D., Barwich, A.S., Malnic, B., and Saraiva, L.R. (2021). Odor coding in the mammalian olfactory epithelium. *Cell Tissue Res.* 383, 445–456.
- Lee, H.K., Park, S.J., Oh, H.J., Kim, J.W., Bae, H.S., and Park, J.C. (2012). Expression pattern, subcellular localization, and functional implications of ODAM in ameloblasts, odontoblasts, osteoblasts, and various cancer cells. *Gene Expr. Patterns* 12, 102–108.
- Leung, C.T., Coulombe, P.A., and Reed, R.R. (2007). Contribution of olfactory neural stem cells to tissue maintenance and regeneration. *Nat. Neurosci.* 10, 720–726.
- Li, H., Handsaker, B., Wysoker, A., Fennell, T., Ruan, J., Homer, N., Marth, G., Abecasis, G., and Durbin, R.; 1000 Genome Project Data Processing Subgroup (2009). The sequence alignment/map format and SAMtools. *Bioinformatics* 25, 2078–2079.
- Liaw, A., and Wiener, M. (2002). Classification and regression by randomForest. *R News* 2, 18–22.
- Liberles, S.D., and Buck, L.B. (2006). A second class of chemosensory receptors in the olfactory epithelium. *Nature* 442, 645–650.
- Ling, G., Gu, J., Genter, M.B., Zhuo, X., and Ding, X. (2004). Regulation of cytochrome P450 gene expression in the olfactory mucosa. *Chem. Biol. Interact.* 147, 247–258.
- Liu, L., Tang, L., Dong, W., Yao, S., and Zhou, W. (2016). An overview of topic modeling and its current applications in bioinformatics. *Springerplus* 5, 1608.
- Liu, X., Su, X., Wang, F., Huang, Z., Wang, Q., Li, Z., Zhang, R., Wu, L., Pan, Y., Chen, Y., et al. (2011). ODORactor: a web server for deciphering olfactory coding. *Bioinformatics* 27, 2302–2303.
- Loader, C. (2007). R Package “lmer”: Local Regression, Likelihood and Density Estimation (Version 1).
- Lun, A.T., McCarthy, D.J., and Marioni, J.C. (2016). A step-by-step workflow for low-level analysis of single-cell RNA-seq data with bioconductor. *F1000Res.* 5, 2122.
- Ma, M., and Shepherd, G.M. (2000). Functional mosaic organization of mouse olfactory receptor neurons. *Proc. Natl. Acad. Sci. U S A* 97, 12869–12874.
- Malnic, B., Godfrey, P.A., and Buck, L.B. (2004). The human olfactory receptor gene family. *Proc. Natl. Acad. Sci. U S A* 101, 2584–2589.

- Malnic, B., Hirono, J., Sato, T., and Buck, L.B. (1999). Combinatorial receptor codes for odors. *Cell* 96, 713–723.
- Manoel, D., Makhoul, M., Arayata, C.J., Sathappan, A., Da'as, S., Abdelrahman, D., Selvaraj, S., Hasnah, R., Mainland, J.D., Gerkin, R.C., et al. (2021). Deconstructing the mouse olfactory percept through an ethological atlas. *Curr. Biol.* 31, 2809–2818.e3.
- Marchand, J.E., Yang, X., Chikaraishi, D., Krieger, J., Breer, H., and Kauer, J.S. (2004). Olfactory receptor gene expression in tiger salamander olfactory epithelium. *J. Comp. Neurol.* 474, 453–467.
- McInnes, L., Healy, J., and Melville, J. (2018). UMAP: uniform manifold approximation and projection for dimension reduction. Preprint at arXiv. <https://doi.org/10.48550/arXiv.1802.03426>.
- Miyamichi, K., Serizawa, S., Kimura, H.M., and Sakano, H. (2005). Continuous and overlapping expression domains of odorant receptor genes in the olfactory epithelium determine the dorsal/ventral positioning of glomeruli in the olfactory bulb. *J. Neurosci.* 25, 3586–3592.
- Miyawaki, A., Homma, H., Tamura, H., Matsui, M., and Mikoshiba, K. (1996). Zonal distribution of sulfotransferase for phenol in olfactory sustentacular cells. *EMBO J.* 15, 2050–2055.
- Miyawaki, A., Matsushita, F., Ryo, Y., and Mikoshiba, K. (1994). Possible pheromone-carrier function of two lipocalin proteins in the vomeronasal organ. *EMBO J.* 13, 5835–5842.
- Mombaerts, P., Wang, F., Dulac, C., Chao, S.K., Nemes, A., Mendelsohn, M., Edmondson, J., and Axel, R. (1996). Visualizing an olfactory sensory map. *Cell* 87, 675–686.
- Monahan, K., Schieren, I., Cheung, J., Mumbey-Wafula, A., Monuki, E.S., and Lomvardas, S. (2017). Cooperative interactions enable singular olfactory receptor expression in mouse olfactory neurons. *Elife* 6, e28620.
- Mozell, M.M. (1966). The spatiotemporal analysis of odorants at the level of the olfactory receptor sheet. *J. Gen. Physiol.* 50, 25–41.
- Nara, K., Saraiva, L.R., Ye, X., and Buck, L.B. (2011). A large-scale analysis of odor coding in the olfactory epithelium. *J. Neurosci.* 31, 9179–9191.
- Nguyen, M.Q., Zhou, Z., Marks, C.A., Ryba, N.J., and Belluscio, L. (2007). Prominent roles for odorant receptor coding sequences in allelic exclusion. *Cell* 131, 1009–1017.
- Nickell, M.D., Breheny, P., Stromberg, A.J., and McClintock, T.S. (2012). Genomics of mature and immature olfactory sensory neurons. *J. Comp. Neurol.* 520, 2608–2629.
- Niimura, Y., Matsui, A., and Touhara, K. (2014). Extreme expansion of the olfactory receptor gene repertoire in African elephants and evolutionary dynamics of orthologous gene groups in 13 placental mammals. *Genome Res.* 24, 1485–1496.
- Niimura, Y., Matsui, A., and Touhara, K. (2018). Acceleration of olfactory receptor gene loss in primate evolution: possible link to anatomical change in sensory systems and dietary transition. *Mol. Biol. Evol.* 35, 1437–1450.
- Norlin, E.M., Alenius, M., Gussing, F., Hagglund, M., Vedin, V., and Bohm, S. (2001). Evidence for gradients of gene expression correlating with zonal topography of the olfactory sensory map. *Mol. Cell. Neurosci.* 18, 283–295.
- Octura, J.E.R., Maeda, K.I., and Wakabayashi, Y. (2018). Structure and zonal expression of olfactory receptors in the olfactory epithelium of the goat, *Capra hircus*. *J. Vet. Med. Sci.* 80, 913–920.
- Oka, Y., Katada, S., Omura, M., Suwa, M., Yoshihara, Y., and Touhara, K. (2006). Odorant receptor map in the mouse olfactory bulb: *in vivo* sensitivity and specificity of receptor-defined glomeruli. *Neuron* 52, 857–869.
- Oka, Y., Kobayakawa, K., Nishizumi, H., Miyamichi, K., Hirose, S., Tsuboi, A., and Sakano, H. (2003). O-MACS, a novel member of the medium-chain acyl-CoA synthetase family, specifically expressed in the olfactory epithelium in a zone-specific manner. *Eur. J. Biochem.* 270, 1995–2004.
- Oka, Y., Omura, M., Kataoka, H., and Touhara, K. (2004). Olfactory receptor antagonism between odorants. *EMBO J.* 23, 120–126.
- Oka, Y., Takai, Y., and Touhara, K. (2009). Nasal airflow rate affects the sensitivity and pattern of glomerular odorant responses in the mouse olfactory bulb. *J. Neurosci.* 29, 12070–12078.
- Omura, M., and Mombaerts, P. (2015). Trpc2-expressing sensory neurons in the mouse main olfactory epithelium of type B express the soluble guanylate cyclase Gucy1b2. *Mol. Cell. Neurosci.* 65, 114–124.
- Pacifico, R., Dewan, A., Cawley, D., Guo, C., and Bozza, T. (2012). An olfactory subsystem that mediates high-sensitivity detection of volatile amines. *Cell Rep.* 2, 76–88.
- Paradis, E., Claude, J., and Strimmer, K. (2004). APE: analyses of phylogenetics and evolution in R language. *Bioinformatics* 20, 289–290.
- Park, J., Levic, D.S., Sumigay, K.D., Bagwell, J., Eroglu, O., Block, C.L., Eroglu, C., Barry, R., Lickwar, C.R., Rawls, J.F., et al. (2019). Lysosome-rich enterocytes mediate protein absorption in the vertebrate gut. *Dev. Cell* 51, 7–20.e6.
- Peluso, C.E., Jang, W., Drager, U.C., and Schwob, J.E. (2012). Differential expression of components of the retinoic acid signaling pathway in the adult mouse olfactory epithelium. *J. Comp. Neurol.* 520, 3707–3726.
- Peng, G., Suo, S., Chen, J., Chen, W., Liu, C., Yu, F., Wang, R., Chen, S., Sun, N., Cui, G., et al. (2016). Spatial transcriptome for the molecular annotation of lineage fates and cell identity in mid-gastrula mouse embryo. *Dev. Cell* 36, 681–697.
- Pfister, P., Smith, B.C., Evans, B.J., Brann, J.H., Trimmer, C., Sheikh, M., Arroyave, R., Reddy, G., Jeong, H.Y., Raps, D.A., et al. (2020). Odorant receptor inhibition is fundamental to odor encoding. *Curr. Biol.* 30, 2574–2587.e6.
- Rather, T.A., Kumar, S., and Khan, J.A. (2020). Multi-scale habitat modelling and predicting change in the distribution of tiger and leopard using random forest algorithm. *Sci. Rep.* 10, 11473.
- Rehurek, R., and Sojka, P. (2010). Software framework for topic modelling with large corpora. In *Proceedings of the LREC 2010 Workshop on New Challenges for NLP Frameworks (ELRA)*, pp. 45–50.
- Repicky, S.E., and Luetje, C.W. (2009). Molecular receptive range variation among mouse odorant receptors for aliphatic carboxylic acids. *J. Neurochem.* 109, 193–202.
- Ressler, K.J., Sullivan, S.L., and Buck, L.B. (1993). A zonal organization of odorant receptor gene expression in the olfactory epithelium. *Cell* 73, 597–609.
- Ressler, K.J., Sullivan, S.L., and Buck, L.B. (1994). Information coding in the olfactory system: evidence for a stereotyped and highly organized epitope map in the olfactory bulb. *Cell* 79, 1245–1255.
- Rygg, A.D., Van Valkenburgh, B., and Craven, B.A. (2017). The influence of sniffing on airflow and odorant deposition in the canine nasal cavity. *Chem. Senses* 42, 683–698.
- Saito, H., Kubota, M., Roberts, R.W., Chi, Q., and Matsunami, H. (2004). RTP family members induce functional expression of mammalian odorant receptors. *Cell* 119, 679–691.
- Saito, H., Nishizumi, H., Suzuki, S., Matsumoto, H., Ieki, N., Abe, T., Kiyonari, H., Morita, M., Yokota, H., Hirayama, N., et al. (2017). Immobility responses are induced by photoactivation of single glomerular species responsive to fox odour TMT. *Nat. Commun.* 8, 16011.
- Saraiva, L.R., Ahuja, G., Ivandic, I., Syed, A.S., Marioni, J.C., Korsching, S.I., and Logan, D.W. (2015a). Molecular and neuronal homology between the olfactory systems of zebrafish and mouse. *Sci. Rep.* 5, 11487.
- Saraiva, L.R., Ibarra-Soria, X., Khan, M., Omura, M., Scialdone, A., Mombaerts, P., Marioni, J.C., and Logan, D.W. (2015b). Hierarchical deconstruction of mouse olfactory sensory neurons: from whole mucosa to single-cell RNA-seq. *Sci. Rep.* 5, 18178.
- Saraiva, L.R., Riveros-McKay, F., Mezzavilla, M., Abou-Moussa, E.H., Arayata, C.J., Makhoul, M., Trimmer, C., Ibarra-Soria, X., Khan, M., Van Gerven, L., et al. (2019). A transcriptomic atlas of mammalian olfactory mucosae reveals an evolutionary influence on food odor detection in humans. *Sci. Adv.* 5, eaax0396.

- Schmal, C., Myung, J., Herzel, H., and Bordyugov, G. (2017). Moran's I quantifies spatio-temporal pattern formation in neural imaging data. *Bioinformatics* 33, 3072–3079.
- Schoenfeld, T.A., and Cleland, T.A. (2006). Anatomical contributions to odorant sampling and representation in rodents: zoning in on sniffing behavior. *Chem. Senses* 31, 131–144.
- Scott, J.W., and Scott-Johnson, P.E. (2002). The electroolfactogram: a review of its history and uses. *Microsc. Res. Tech.* 58, 152–160.
- Scott, J.W., Sherrill, L., Jiang, J., and Zhao, K. (2014). Tuning to odor solubility and sorption pattern in olfactory epithelial responses. *J. Neurosci.* 34, 2025–2036.
- Secundo, L., Snitz, K., and Sobel, N. (2014). The perceptual logic of smell. *Curr. Opin. Neurobiol.* 25, 107–115.
- Secundo, L., Snitz, K., Weissler, K., Pinchover, L., Shoenfeld, Y., Loewenthal, R., Agmon-Levin, N., Frumin, I., Bar-Zvi, D., Shushan, S., et al. (2015). Individual olfactory perception reveals meaningful nonolfactory genetic information. *Proc. Natl. Acad. Sci. U S A* 112, 8750–8755.
- Shin, Y., Won, Y., Yang, J.I., and Chun, J.S. (2019). CYTL1 regulates bone homeostasis in mice by modulating osteogenesis of mesenchymal stem cells and osteoclastogenesis of bone marrow-derived macrophages. *Cell Death Dis.* 10, 47.
- Shirasu, M., Yoshikawa, K., Takai, Y., Nakashima, A., Takeuchi, H., Sakano, H., and Touhara, K. (2014). Olfactory receptor and neural pathway responsible for highly selective sensing of musk odors. *Neuron* 81, 165–178.
- Shirokova, E., Schmiedeberg, K., Bedner, P., Niessen, H., Willecke, K., Raguse, J.D., Meyerhof, W., and Krautwurst, D. (2005). Identification of specific ligands for orphan olfactory receptors. G protein-dependent agonism and antagonism of odorants. *J. Biol. Chem.* 280, 11807–11815.
- Simes, R.J. (1986). An improved Bonferroni procedure for multiple tests of significance. *Biometrika* 73, 751–754.
- Springer, M.S., Emerling, C.A., Gatesy, J., Randall, J., Collin, M.A., Hecker, N., Hiller, M., and Delsuc, F. (2019). Odontogenic ameloblast-associated (ODAM) is inactivated in toothless/enamelless placental mammals and toothed whales. *BMC Evol. Biol.* 19, 31.
- Spuch, C., Ortolano, S., and Navarro, C. (2012). LRP-1 and LRP-2 receptors function in the membrane neuron. Trafficking mechanisms and proteolytic processing in Alzheimer's disease. *Front. Physiol.* 3, 269.
- Strotmann, J., Wanner, I., Krieger, J., Raming, K., and Breer, H. (1992). Expression of odorant receptors in spatially restricted subsets of chemosensory neurones. *Neuroreport* 3, 1053–1056.
- Sullivan, S.L., Adamson, M.C., Ressler, K.J., Kozak, C.A., and Buck, L.B. (1996). The chromosomal distribution of mouse odorant receptor genes. *Proc. Natl. Acad. Sci. U S A* 93, 884–888.
- Taddy, M. (2012). On estimation and selection for topic models. In *Proceedings of the Fifteenth International Conference on Artificial Intelligence and Statistics*, D.L. Neil and G. Mark, eds., pp. 1184–1193, *Proceedings of Machine Learning Research: PMLR*.
- Tan, L., and Xie, X.S. (2018). A near-complete spatial map of olfactory receptors in the mouse main olfactory epithelium. *Chem. Senses* 43, 427–432.
- Tietjen, I., Rihel, J., and Dulac, C.G. (2005). Single-cell transcriptional profiles and spatial patterning of the mammalian olfactory epithelium. *Int. J. Dev. Biol.* 49, 201–207.
- Tietjen, I., Rihel, J.M., Cao, Y., Koentges, G., Zakhary, L., and Dulac, C. (2003). Single-cell transcriptional analysis of neuronal progenitors. *Neuron* 38, 161–175.
- Trimmer, C., and Mainland, J.D. (2017). Simplifying the odor landscape. *Chem. Senses* 42, 177–179.
- Vassar, R., Chao, S.K., Sitcheran, R., Nunez, J.M., Vosshall, L.B., and Axel, R. (1994). Topographic organization of sensory projections to the olfactory bulb. *Cell* 79, 981–991.
- Vassar, R., Ngai, J., and Axel, R. (1993). Spatial segregation of odorant receptor expression in the mammalian olfactory epithelium. *Cell* 74, 309–318.
- Vedin, V., Molander, M., Bohm, S., and Berghard, A. (2009). Regional differences in olfactory epithelial homeostasis in the adult mouse. *J. Comp. Neurol.* 513, 375–384.
- von der Weid, B., Rossier, D., Lindup, M., Tuberosa, J., Widmer, A., Col, J.D., Kan, C., Carleton, A., and Rodriguez, I. (2015). Large-scale transcriptional profiling of chemosensory neurons identifies receptor-ligand pairs *in vivo*. *Nat. Neurosci.* 18, 1455–1463.
- Wang, Q., Titlow, W.B., McClintock, D.A., Stromberg, A.J., and McClintock, T.S. (2017). Activity-Dependent gene expression in the mammalian olfactory epithelium. *Chem. Senses* 42, 611–624.
- Wang, S.S., Lewcock, J.W., Feinstein, P., Mombaerts, P., and Reed, R.R. (2004). Genetic disruptions of O/E2 and O/E3 genes reveal involvement in olfactory receptor neuron projection. *Development* 131, 1377–1388.
- Wang, T., Wang, Z.Y., Zeng, L.Y., Gao, Y.Z., Yan, Y.X., and Zhang, Q. (2020). Down-regulation of ribosomal protein rps21 inhibits invasive behavior of osteosarcoma cells through the inactivation of MAPK pathway. *Cancer Manag. Res.* 12, 4949–4955.
- Weth, F., Nadler, W., and Korsching, S. (1996). Nested expression domains for odorant receptors in zebrafish olfactory epithelium. *Proc. Natl. Acad. Sci. U S A* 93, 13321–13326.
- Whitby-Logan, G.K., Weech, M., and Walters, E. (2004). Zonal expression and activity of glutathione S-transferase enzymes in the mouse olfactory mucosa. *Brain Res.* 995, 151–157.
- Wolf, F.A., Angerer, P., and Theis, F.J. (2018). SCANPY: large-scale single-cell gene expression data analysis. *Genome Biol.* 19, 15.
- Yang, L.M., Huh, S.H., and Ornitz, D.M. (2018). FGF20-expressing, wnt-responsive olfactory epithelial progenitors regulate underlying turbinate growth to optimize surface area. *Dev. Cell* 46, 564–580.e5.
- Yoshihara, Y., Kawasaki, M., Tamada, A., Fujita, H., Hayashi, H., Kagamiyama, H., and Mori, K. (1997). OCAM: a new member of the neural cell adhesion molecule family related to zone-to-zone projection of olfactory and vomeronasal axons. *J. Neurosci.* 17, 5830–5842.
- Yoshikawa, K., Nakagawa, H., Mori, N., Watanabe, H., and Touhara, K. (2013). An unsaturated aliphatic alcohol as a natural ligand for a mouse odorant receptor. *Nat. Chem. Biol.* 9, 160–162.
- Yoshikawa, K., and Touhara, K. (2009). Myr-Ric-8A enhances G(alpha15)-mediated Ca²⁺ response of vertebrate olfactory receptors. *Chem. Senses* 34, 15–23.
- Yoshikawa, K., Wang, H., Jaen, C., Haneoka, M., Saito, N., Nakamura, J., Adappa, N.D., Cohen, N.A., and Dalton, P. (2018). The human olfactory cleft mucus proteome and its age-related changes. *Sci. Rep.* 8, 17170.
- Yu, T.T., McIntyre, J.C., Bose, S.C., Hardin, D., Owen, M.C., and McClintock, T.S. (2005). Differentially expressed transcripts from phenotypically identified olfactory sensory neurons. *J. Comp. Neurol.* 483, 251–262.
- Yu, Y., de March, C.A., Ni, M.J., Adipietro, K.A., Golebiowski, J., Matsunami, H., and Ma, M. (2015). Responsiveness of G protein-coupled odorant receptors is partially attributed to the activation mechanism. *Proc. Natl. Acad. Sci. U S A* 112, 14966–14971.
- Zapiec, B., and Mombaerts, P. (2020). The zonal organization of odorant receptor gene choice in the main olfactory epithelium of the mouse. *Cell Rep.* 30, 4220–4234.e5.
- Zhang, X., Rogers, M., Tian, H., Zhang, X., Zou, D.J., Liu, J., Ma, M., Shepherd, G.M., and Firestein, S.J. (2004). High-throughput microarray detection of olfactory receptor gene expression in the mouse. *Proc. Natl. Acad. Sci. U S A* 101, 14168–14173.
- Zhu, S., Kuek, V., Bennett, S., Xu, H., Rosen, V., and Xu, J. (2019). Protein Cyt1: its role in chondrogenesis, cartilage homeostasis, and disease. *Cell Mol. Life Sci.* 76, 3515–3523.
- Zhuang, H., and Matsunami, H. (2007). Synergism of accessory factors in functional expression of mammalian odorant receptors. *J. Biol. Chem.* 282, 15284–15293.

STAR★METHODS

KEY RESOURCES TABLE

REAGENT or RESOURCE	SOURCE	IDENTIFIER
Antibodies		
Anti-Digoxigenin-AP, Fab fragments	Merck (Roche)	Cat# 11093274910, RRID:AB_514497
Biological samples		
Olfactory mucosae from C57Bl/6J mice (adult males)	The Jackson Laboratory	Stock # 00664
Chemicals, peptides, and recombinant proteins		
30% Hydrogen Peroxide Solution	Merck (Sigma-Aldrich)	Cat. # H1009
Triethanolamine	Merck (Sigma-Aldrich)	Cat. # T58300
Acetic anhydride	Merck (Sigma-Aldrich)	Cat. # 320102
Deionized formamide	Merck (Sigma-Aldrich)	Cat. # F9037
Yeast tRNA	Merck (Roche)	Cat. # 10109495001
Denhardt's solution (50×)	Merck (Sigma-Aldrich)	Cat. # D9905
Dextran sulfate solution (50%)	Merck (Chemicon)	Cat. # S4030
20× SSC	Merck (Calbiochem)	Cat. # 8310-OP
Tween-20	Merck (Sigma-Aldrich)	Cat. # 822184
TSA Blocking Reagent	Perkin-Elmer	Cat. # FP1020
NBT/BCIP Stock Solution	Merck (Roche)	Cat. # 11681451001
Critical commercial assays		
SMART-Seq v4 Ultra Low Input RNA Kit for Sequencing	Clontech (Takara Bio)	Cat. # 634892
Bioanalyzer DNA High-Sensitivity kit	Agilent Technologies	Cat. # 5067-4626
Nextera XT DNA Library Preparation Kit (96 samples)	Illumina	Cat. # FC-131-1096
Nextera XT Index Kit v2 Set A (96 indexes, 384 samples)	Illumina	Cat. # FC-131-2001
pGEM®-T Easy Vector Systems	Promega	Cat. # A1360
DIG RNA Labeling Kit (SP6/T7)	Merck (Roche)	Cat. # 11175025910
ProbeQuant G-50 Micro Columns	Cytiva Biosciences	Cat. # 28903408
Deposited data		
TOMO-seq Olfactory Mucosa dataset	This study	https://www.ebi.ac.uk/arrayexpress/E-MTAB-10211
Single cell RNA-seq data from the Olfactory Mucosa	Fletcher et al., 2017	https://www.ncbi.nlm.nih.gov/geo/query/acc.cgi?acc=GSE95601
Dragon database of molecular descriptors	Taleta S.R.L.	http://www.taleta.mi.it
CellphoneDB ligands and receptors database	Efremova et al., 2020	https://github.com/ventolab/CellphoneDB
Experimental models: Organisms/strains		
Adult male C57Bl/6J mice	The Jackson Laboratory	Stock # 00664
Oligonucleotides		
See “ method details ” section for oligonucleotides	This study	N/A
Software and algorithms		
samtools version 0.1.19-44428cd	Li et al., 2009	http://samtools.sourceforge.net/
htseq-count version 0.11.2	Anders et al., 2014	https://github.com/htseq/htseq/
R 4.1.2	The R Foundation	https://www.r-project.org/

(Continued on next page)

Continued

REAGENT or RESOURCE	SOURCE	IDENTIFIER
Python 3.9.6	Python Software Foundation	https://www.python.org/
Scripts for TOMO-seq data analysis	This study	https://doi.org/10.5281/zenodo.6036047 https://zenodo.org/badge/DOI/10.5281/zenodo.6045897.svg

RESOURCE AVAILABILITY

Lead contact

Further information and requests for resources and data should be directed to and will be fulfilled by the [Lead Contact](#) Luis R. Saraiva (saraivalmr@gmail.com).

Materials availability

This study did not generate new unique reagents.

Data and code availability

RNA-seq raw data have been deposited and are publicly available as of the date of publication at ArrayExpress: E-MTAB-10211. All original code and scripts for the 3D nose atlas shiny app has been deposited at Github and can be found at the Github Repository: <https://doi.org/10.5281/zenodo.6036047><https://zenodo.org/badge/DOI/10.5281/zenodo.6045897.svg>. The 3D nose atlas processed data can be browsed and visualized here: <http://atlas3dnose.helmholtz-muenchen.de:3838/atlas3Dnose>.

Any additional information required to reanalyze the data reported in this paper is available from the lead contacts upon request.

EXPERIMENTAL MODEL AND SUBJECT DETAILS

Animals

The animals used in this study were adult male C57Bl/6J mice (aged 8–14 weeks, The Jackson Laboratory, Stock # 00664) maintained in group-housed conditions on a 12:12 h light:dark schedule (lights on at 0700 hours). Each mouse was randomly assigned for cryosectioning along one of the three cartesian axes.

The use and care of animals used in this study was approved by the Internal Animal Care and Use Committee (IACUC) of Monell Chemical Senses Center, by the IACUC of the University of São Paulo, and by the Wellcome Trust Sanger Institute Animal Welfare and Ethics Review Board in accordance with UK Home Office regulations, the UK Animals (Scientific Procedures) Act of 1986.

METHOD DETAILS

Dissection of the olfactory mucosa, cryosections, and RNA-sequencing

The olfactory mucosa (OM) of 9 mice was carefully dissected, and all the surrounding tissue (including glands and bone) removed – this was necessary to ensure that the transcripts present in the surrounding tissue do not contaminate the RNA isolated from the OM. The OM was then embedded in OCT (Tissue Tek), immediately frozen in dry-ice and kept at -80°C . Each OM was then cryosectioned along each of the 3 cartesian axes: dorsal-ventral (DV, $n = 3$), anterior-posterior (AP, $n = 3$), or lateral-medial-lateral (LML, $N = 3$). Every second cryosections (35 μm thick) was collected into 1.5 mL eppendorf tubes containing 350 μL RLT Plus Buffer (Qiagen) supplemented with 1% 2-mercaptoethanol, immediately frozen in dry-ice and kept at -80°C until extraction. RNA was extracted using the RNeasy Plus Micro Kit (Qiagen), together with a genomic DNA eliminator column and a 30-minute incubation with DNase I (Qiagen). Reverse transcription and cDNA pre-amplification were performed using the SMART-Seq v4 Ultra Low Input RNA Kit for Sequencing (Clontech/Takara). cDNA was harvested and quantified with the Bioanalyzer DNA High-Sensitivity kit (Agilent Technologies). Libraries were prepared using the Nextera XT DNA Sample Preparation Kit and the Nextera Index Kit (Illumina). Multiplexed libraries were pooled and paired-end 150-bp sequencing was performed on the Illumina HiSeq 4000 platform at Sidra Medicine, except for one library (DV-I) for which 125-bp paired-end sequencing was performed on the Illumina HiSeq 2500 platform at the Wellcome Sanger Institute. The raw data are available through ArrayExpress under accession number E-MTAB-10211.

RNA-seq data mapping and gene counting

Reads were aligned to the mm10 mouse genome (release 99). The sequences of the genes “*Xntrpc*” and “*Capn5*” were removed from the genome files as in [Saraiva et al. \(2015b\)](#). The alignment was performed with the software STAR version 2.7.3a ([Dobin et al., 2013](#)). Genome indexes were generated using STAR –runMode genomeGenerate with default parameters. Then, alignment of reads was performed with the following options: –runThreadN 48 –outSAMunmapped Within –outFilterMultimapNmax 1000 –outFilterMismatchNmax 4 –outFilterMatchNmin 100 –alignIntronMax 50000 –alignMatesGapMax 50500 –outSAMstrandField intronMotif –outFilterType BySJout. The resulting SAM files were converted to bam format and sorted using samtools (version 0.1.19-44428cd) ([Li et al.,](#)

2009). The multi mapping reads were eliminated using the same software (samtools view -q 255). Finally, the reads for each gene were counted using htseq-count (version 0.11.2) with the options -m intersection-nonempty -s no -i gene_name -r pos (Anders et al., 2014).

Quality control

We excluded all the samples that fulfilled any of these criteria: they had less than 50% mapped reads, less than 4,000 detected genes, more than 20% mitochondrial reads, less than 10,000 total number of reads, or did not express any of the 3 canonical OSN markers *Omp*, *Cnga* and *Gnal*. This resulted in ~51 good-quality sections along the DV axis (~84% out of the collected sections), ~76 (~91% of total) along the AP axis and ~59 (~93% of total) along the LML axis, as averaged across the three replicates per axis.

Data normalization

Gene expression counts were normalized by reads-per-million (RPM), then genes detected in only one replicate and genes that were detected in less than 10% of all samples along one axis were eliminated. To check the similarity between replicates, we calculated Spearman correlations between the transcriptional profiles of sections along each axis (using the top 1000 Highly Variable Genes per axis). Close positions had the most similar transcriptional profiles (Figure 1C). Afterward, the 3 replicates for each axis were aligned as follows: the top 3,000 highly variable genes (HVGs) from each replicate were identified using the method implemented in the scran library in R (Lun et al., 2016) and the intersection of these 3 groups was used in the next steps. For the replicates' alignment, we took as reference the replicate with the smallest number of slices. We used a sliding window approach that identified the range of consecutive positions on each replicate along which the average value of the Spearman's correlation coefficient computed with the reference replicate over the HVG was maximum (mean Spearman's $Rho = 0.80$, $p < 0.05$). To mitigate batch effects, the level of every gene was scaled in such a way that their average value in each replicate was equal to the average calculated across all replicates. After this scaling transformation, the data was then averaged between replicates. Once the 3 biological replicates were combined, we had 54 sections along the DV axis, 60 along the AP and 56 along the LML. Along the LML axis a symmetric pattern of expression is expected around the central position, where the septal bone is located. To confirm this in our data, first we identified the central position by analyzing the expression pattern of neuronal markers like *Cnga2*, *Omp* and *Gnal*, whose expression is lowest in the area around the septal bone. Indeed, all three marker genes reach a minimum at the same position along the LML axis (slice 28), which we considered to be the center. The expression patterns of ~90% of genes on either side of the central position show a positive correlation, and ~70% reach statistical significance (Spearman's correlation computed on the highly variable genes having more than 50 normalized counts in at least 3 slices), further supporting the hypothesis of the bilateral symmetry. Hence, after replicates were averaged, LML axis was made symmetric averaging positions 1:28 and 56:29. Moreover, *Olfrs* were normalized by the geometric mean of neuronal markers *Omp*, *Gnal* and *Cnga2*, as done previously (Ibarra-Soria et al., 2017).

To verify the presence of a spatial signal, we calculated the Moran's I and the associated p-values for the top 100 Highly Variable genes along each axis using the "Moran.I" function from the "ape" library in R with default parameters (Paradis et al., 2004). The p-values of the genes along each axis were combined with the Simes' method (Simes, 1986) using the function combinePValues from the scran R library (Figure S1E).

Identification of differentially expressed genes and gene clustering

Before testing for differential expression along a given axis, we filtered out genes whose expression levels had low variability. To this aim, for each gene we estimated their highest and lowest expression by taking the average of its three highest and three lowest values respectively. Then, we considered for downstream analyses only the genes that meet either of these two criteria: the highest expression value is greater than or equal to 5 normalized counts and the fold-change between the highest and lowest value is greater than 2; or the difference between the highest and the lowest value is greater than or equal to 4 normalized counts. The expression levels of the genes were binarized according to whether their value was higher or lower than their median expression along the axis. Finally, we used the "ts" function in R to transform the binarized expression values into time series objects, and we applied on them the Ljung-Box test (Box.test function in R with lag = (axis length)-10) which identifies genes with statistically significant autocorrelations, i.e., with non-random expression patterns along an axis. The resulting p-values were adjusted using the FDR method and genes with an FDR < 0.01 were considered as differentially expressed. For the next steps, the \log_{10} normalized expression of differentially expressed genes along each axis was fitted with a local regression using the locfit function in the R library locfit (Loader, 2007). Smoothing was defined in the local polynomial model term of the locfit model using the function "lp" from the same library with the following parameters: nn = 1 (Nearest neighbor component of the smoothing parameter) and deg = 2 (degree of polynomial). The fitted expression values of these genes along each axis were normalized between 0 and 1. Clustering was performed separately for each axis on the fitted and normalized patterns of the differentially expressed genes. We used the R function "hclust" to perform hierarchical clustering on the gene expression patterns, with a Spearman's correlation-based distance (defined as $\sqrt{0.5(1-\rho)}$) and the "average" aggregation method. The number of clusters were defined with the cutreeDynamic function from the dynamicTreeCut R library, with the parameters minClusterSize = 50, method = "hybrid" and deepSplit = 0. To visualize the data in two dimensions, we applied the UMAP dimensionality reduction algorithm (umap function in the R library umap with default options; see Figure 2D) (Becht et al., 2018; McInnes et al., 2018). To analyze the relationship between the expression patterns of genes along different axes, we computed the

intersections of the gene clusters between any pair of axes. The expected number of elements in each intersection under the assumption of independent sets is given by:

$$|A \cap B|_{exp} = \frac{|A||B|}{|A \cup B|}$$

where A and B indicate the sets of genes in two clusters identified along two different axes and $|\cdot|$ indicates the cardinality of a set (i.e., the number of its elements). The ratio between the observed and the expected number of elements in the intersection $|A \cap B|_{obs} / |A \cap B|_{exp}$ quantifies the enrichment/depletion of genes having a given pair of patterns across two axes with respect to the random case. The \log_2 values of $(1 + |A \cap B|_{obs} / |A \cap B|_{exp})$ are shown in Figure 2F.

Combining Tomo-seq with single-cell RNA-seq data

The TPM (transcripts per million)-normalized single cell RNA-seq (scRNA-seq) data collected from mouse olfactory epithelium available from Fletcher et al. (2017) was used to identify cell-type specific genes. To this aim, we computed the average expression level for each cell type in the scRNA-seq dataset for all the differentially expressed genes that we identified in our TOMO-seq data. The genes with an average expression above 100 TPM in mOSNs and below 10 TPM in all other cell types were considered mOSN-specific. Conversely, genes with an average expression above 100 TPM in any of the non-mOSN cell types and below 10 in mOSNs were considered to be specific for non-mOSN cells.

Gene ontology (GO) enrichment analysis

GO Enrichment analyses were performed using the GOrilla online tool (<http://cbl-gorilla.cs.technion.ac.il>) with the option “Two unranked lists of genes (target and background lists)”. For each axis, we used as background list the list of the genes we tested.

Cell type deconvolution analysis

To perform cell type deconvolution analysis, we used a previously published single-cell RNA-seq (scRNA-seq) data from the mouse OM (Fletcher et al., 2017). First, the cells included in unclassified clusters were removed and the data was rescaled using the function “pp.log1p” from the scanpy library (Wolf et al., 2018). Then, we obtained 2000 highly variable genes using the function “pp.highly_variable_genes” (scanpy library). In the following analysis, we merged clusters of similar cell populations and considered the following 6 cell types: 1-HBC = HBC1+HBC2+HBC3; 2-INP = INP1+INP2+INP3; 3-GBC = GBC, 4-SC = mSC + iSC, 5-OSN = iOSN + mOSN, 6-MVC = MVC1+MVC2.

This scRNA-seq data was used as input for the AutoGeneS algorithm (Aliee and Theis, 2021). The cell type assignment as well as the list of highly variable genes were passed as input to the function “ag.init” from AutogeneS, and then we estimated the optimal subset of genes to perform cell type deconvolution with the function “ag.optimize” (with parameters: “ngen” = 5000, “nfeatures” = 400 and “mode” = “fixed”). Finally, we deconvolved the Tomo-seq data along the three axes with the function “ag.deconvolve” using Nu Support Vector regression models (“model” = “nusvr”). The results were normalized such that the sums of cell type proportions per slice is equal to 1 (Figure S2F). To identify the cell types with non-random spatial distribution along the axes, we applied the Ljung-Box test as explained above (section “identification of differentially expressed genes and gene clustering”); the p values are reported in Table S2.

Identification of ligands and receptors associated with the NfiA, NfiB or NfiX transcription factors

The genes in the CellphoneDB ligands and receptor database (Efremova et al., 2020) that were among our spatially differentially expressed genes were selected and Spearman correlation tests between their 1D expression patterns and the 1D patterns for the Nfi transcription factors were performed. Correlation coefficients from the three axes were averaged and FDRs from the 3 axes were combined with the Simes’ method (Simes, 1986) using the function combinePValues from the scan R library. Combined FDR values <0.01 were taken as significant.

3D spatial reconstruction

The olfactory mucosa shape was obtained from publicly available images of the mouse nasal cavity along the posterior to the anterior axis published in Barrios et al. (2014). The area of the slices corresponding to the OM was manually selected and images of their silhouettes were made. Those images were then transformed into binary matrices having 1’s in the area occupied by the OM and 0’s in the remaining regions. The binary matrices were rescaled to match the spatial resolution in our dataset, which is composed of 54 voxels along the DV axis, 56 along the LML axis and 60 along the AP axis. Finally, matrices were piled in a 3D array in R to obtain an in-silico representation of the 3D shape of the OM, which, in total, was composed of 77,410 voxels. To perform the 3D reconstruction of the expression pattern for a given gene, first we normalized its expression levels by the volume of the slice at each corresponding position along the three axes, which was estimated using our 3D in silico representation of the OM. Then, we rescaled the data in such a way that the sum of the expression levels along each axis was equal to the average expression computed across the whole dataset. This rescaled dataset together with the binary matrix representing the 3D OM shape was used as input of the Iterative Proportional Fitting algorithm, which produced an estimation of the expression level of a gene in each voxel (Junker et al., 2014). Iterations stopped when the differences between the true and the reconstructed 1D values summed across the three axes was smaller than 1.

Definition of zones by topic modelling

In order to identify zones, we fitted a Latent Dirichlet Allocation (LDA) (Blei et al., 2003) algorithm to the 3D gene expression patterns (in log₁₀ scale) of the differentially expressed *Olfrs* (689 *Olfrs* x 77,410 voxels).

The LDA algorithm was originally employed for document classification: based on the words included in each document, LDA can identify "topics", in which the documents can then be classified. Using this linguistic analogy, in our application of LDA, we considered the genes as "documents", and the spatial locations as "words", with the matrix of gene expression levels being the analogous of the "bag-of-words" matrix (Liu et al., 2016). In this representation, the zones are the equivalent of "topics", and they are automatically identified by LDA. We used the LDA implementation included in the R package "Countclust" (Dey et al., 2017), developed based on the "mapprox" library (Taddy, 2012), which performs a maximum a posteriori estimation to for model fitting. LDA was run for all possible numbers of topics $K \in [2, 9]$. The following parameters were chosen: convergence tolerance = 0.1; max time optimization step = 180 seconds; $n_{\text{init}} = 3$. For each number of topics k , three independent runs were performed with different starting points, in order to avoid biases due to the choice of the initial condition. We estimated the number of topics by computing the log likelihood for each value of $K \in [2, 9]$. As seen in Figure S3A, while the log-likelihood is a monotonically increasing function of the number of topic (as expected), for a number of topics around ~5 it shows a "knee" and starts to increase more slowly. This suggests that ~5 is the minimal number of topics needed to describe the complexity of the data without overfitting. Hence, we fix a number of topics equal to 5; however, we also verified that all our conclusions remain substantially unaffected if a different number of topics is chosen.

After running LDA with $K = 5$, we retrieved the model output, which consists of two probability distributions: the first is $P(\text{position} | k)$ with $k \in [1, 5]$, which is the conditional probability distribution defining the topic k ; the second probability distribution is $P(k | \text{gene})$, namely the probability distribution that quantifies the degrees of belonging of a given gene to the topics $k \in [1, 5]$. With these probability distributions, we can identify the spatial positions that form each topic and how the different topics can be combined to generate the spatial expression pattern of each gene.

Being a generative model, once trained, LDA can also decompose into topics the spatial expression patterns of genes that were not used during the training procedure. We exploited this feature of LDA to estimate the degrees of belonging of non-olfactory receptor genes. To this aim, we utilized an algorithm based on the python gensim library `Lda.Model.inference` function (Rehurek and Sojka, 2010), using as input the estimated probability distribution $P(\text{position} | k)$ with $k \in [1, 5]$. The model fitting was performed using the Open Computing Cluster for Advanced data Manipulation (OCCAM), the High-Performance Computer designed and managed in collaboration between the University of Torino and the Torino division of the Istituto Nazionale di Fisica Nucleare (Aldinucci et al., 2017).

Definition of *Olfr* 3D indexes via diffusion pseudo-time

As explained in the section above, we can describe the spatial expression pattern of each gene through a set of five numbers, which represent the degrees of belonging to the five topics identified by LDA. We applied a diffusion map (Haghverdi et al., 2015) to the degrees of belonging of the *Olfrs* to visualize them in two dimensions by using the "DiffusionMap" function from the "destiny" R package (Angerer et al., 2016) (with distance = "rankcor" and default parameters). In this two-dimensional map, the *Olfrs* are approximately distributed along a curve that joins the most dorsal/medial genes (those in zones 1–2) with those that are more ventral/lateral (zones 3–5). To track the position of the genes along this curve, we computed a diffusion pseudo-time (DPT) coordinate (Haghverdi et al., 2016) with the "DPT" function from the "destiny" R package (taking as starting point the gene with the smallest first diffusion component among the genes suggested by the function `find_tips` from the same package). In order to make the indexes go from Dorsal to Ventral, as in previous studies (Miyamichi et al., 2005), we reversed the order of the DPT coordinates by subtracting the maximum coordinate from all coordinates and multiplying them by (–1). By doing this, we obtained for each *Olfr* an index, which we called 3D index, representing its spatial expression pattern in the 3D space: more dorsal/medial genes (zones 1–2) have smaller 3D indexes than *Olfrs* expressed in the ventral/lateral regions (zones 3–5).

Prediction of zone index for undetected *Olfrs* with Random Forest

We fitted a Random Forest model to the 3D indexes of 681 of the 689 *Olfrs* we characterized with our dataset (i.e., those that are located in genomic clusters). The following nine features of each *Olfr* were used as predictors: genomic position (i.e., gene starting position divided by chromosome length); genomic cluster; genomic cluster length; number of *Olfrs* in the genomic cluster; number of enhancers in the genomic cluster; cluster position (i.e., starting position of the cluster divided by the chromosome length); distance to the closest enhancer; gene position within the cluster (i.e., the distance of the gene starting position from the end of the cluster divided by the cluster length); and phylogenetic class. These features were computed using the mm10 mouse genome in Biomart (Kinsella et al., 2011), while the list of enhancers and the genomic clusters assigned to each *Olfr* were taken from Monahan et al. (2017). The Random Forest model was fitted with the function "randomForest" (R library "randomForest" (Liaw and Wiener, 2002), with option "na.action = na.omit"). Afterward, we performed a cross-validation test with the function "rf.crossValidation" from the "rfUtilities" package (Rather et al., 2020) with default parameters. Over 100 cross-validation iterations, the root mean square error (RMSE) was $\leq 10\%$ of the mean 3D index. The feature importance was computed with the "importance" function from the randomForest library with default parameters. Finally, the Random Forest model trained on the 681 *Olfrs* was used to predict the 3D indexes of 697 *Olfrs* that were too lowly expressed or were undetected in our dataset. Overall, we were able to compute or predict with Random Forest a 3D index for all the *Olfrs* annotated in the mouse genome, except for 28 of them that do not have any genomic cluster assigned. To quantify the consistency between our *Olfr* 3D indexes and indexes defined previously, we calculated the Spearman's correlation

coefficients between our indexes and those defined in three previous studies (Miyamichi et al., 2005; Tan and Xie, 2018; Zapiec and Mombaerts, 2020) (see Figures 4G, S4B, and S4C).

Odorant information and Olfr-ligand pairs

All odorant structures and associated CAS numbers were retrieved from either Sigma-Aldrich (www.sigmaaldrich.com) or PubChem (<https://pubchem.ncbi.nlm.nih.gov>). A comprehensive catalog of the cognate mouse Olfr-ligand pairs was collected (last update: March 2021) by combining data from the ODORactor database (Liu et al., 2011) and additional literature sources (Abaffy et al., 2006; Araneda et al., 2004; Bozza et al., 2002; Dunkel et al., 2014; Floriano et al., 2000; Gaillard et al., 2002; Godfrey et al., 2004; Grosmaître et al., 2006, 2009; Jiang et al., 2015; Jones et al., 2019; Kajiya et al., 2001; Malnic et al., 1999, 2004; Nara et al., 2011; Nguyen et al., 2007; Oka et al., 2004, 2006, 2009; Pfister et al., 2020; Repicky and Luetje, 2009; Saito et al., 2004, 2017; Saraiva et al., 2019; Shirasu et al., 2014; Shirokova et al., 2005; von der Weid et al., 2015; Yoshikawa et al., 2013; Yoshikawa and Touhara, 2009; Yu et al., 2015; Zhuang and Matsunami, 2007).

This catalog includes 738 Olfr-ligand interactions for a total of 153 Olfrs and 221 odorants. These 153 Olfrs include 100 spatial Olfrs in our dataset and for which we have 3D indexes, and 49 additional Olfrs with predicted 3D indexes (see above). Next, we checked whether Olfrs pairs sharing at least one cognate ligand have more similar spatial expression patterns than pairs not sharing ligands. To do this, we computed the absolute values of the differences between the 3D indexes (Δ) of 1706 pairs of ORs sharing at least one odorant and 9,922 pairs of ORs that are known to bind to different odorants (Figure 6B). The two sets of Δ values were significantly different (Mann-Whitney U test, p value $< 2 \times 10^{-16}$). This test remained significant when excluding Olfrs for which 3D indexes were estimated by the Random Forests model (p value $< 2 \times 10^{-16}$), and also when excluding class I Olfrs (p value $< 2 \times 10^{-16}$).

Correlation analysis of physico-chemical descriptors with 3D index

Physicochemical descriptors for ligands were obtained from the Dragon 6.0 software (<http://www.taletmi.it/>). After removing the descriptors showing 0 variance, a table of 1911 descriptors for 205 ligands was obtained. In addition to these, we estimated the air/mucus partition coefficients (K_{am}) of the odorants as done previously (Rygg et al., 2017; Scott et al., 2014). Briefly, we calculated the air/water partition coefficients (K_{aw}) for each odorant from the Henry's Law constants obtained using the HENRYWIN model in the US EPA Estimation Program Interface (EPI) Suite (version 4.11; www.epa.gov/oppt/exposure/pubs/episuite.htm). Then, we computed the air/mucus partition coefficients (K_{am}) according to the formula:

$$\text{Log}(K_{am}) = 0.524 \cdot \text{Log}(K_{aw}) \cdot \text{Log}(K_{ow})$$

where K_{ow} indicates the octanol/water partition coefficient, which were obtained using the KOWWIN model in the EPI Suite.

To increase the robustness of our correlation analysis, we removed the descriptors with 20 or more identical values across our set of ligands, and we initially considered only the ligands having 2 or more known cognate receptors; these filters gave us 1,210 descriptors (including K_{am}) for 101 ligands.

We performed Spearman's correlation tests between the physicochemical descriptors and mean 3D index of the cognate Olfrs, and we considered as statistically significant those correlations with FDR < 0.05 (see Table S6). The descriptors with the largest correlation coefficients were K_{am} ($\rho = 0.55$, $p = 1 \times 10^{-7}$) and ATSC2s (Centred Broto-Moreau Autocorrelation of lag 2 weighted by I-state, $\rho = -0.56$, $p = 2 \times 10^{-7}$). We obtained statistically significant correlations between K_{am} and the mean 3D indexes also when excluding Olfrs with 3D indexes predicted by Random Forest ($\rho = 0.48$, p value $= 2 \times 10^{-6}$, based on 87 ligands; Figure S5B) or excluding class I Olfrs ($\rho = 0.5$, p value $= 1 \times 10^{-7}$, based on 101 ligands; Figure S5C).

In-situ hybridization

In-situ hybridization was basically performed as previously described (Ibarra-Soria et al., 2017). Adult 12-week-old male C57BL/6J mice anesthetized, and then perfused with 4% paraformaldehyde. The snouts containing the OM were dissected out, decalcified in RNase-free 0.45M EDTA solution (in $1 \times$ PBS) for two weeks – the bone and tissue encapsulating the OM are necessary to preserve the OM tissue integrity during the ISH. Next, the decalcified snouts were cryoprotected in RNase-free 30% sucrose solution ($1 \times$ PBS), dried, embedded in OCT embedding medium, and frozen at -80°C . Sequential $16 \mu\text{m}$ sections were prepared with a cryostat and the sections were hybridized to digoxigenin-labeled cRNA probes prepared from the different genes using the following oligonucleotides: *Cytl* (5'-AAAGACACTACCTCTGTTGCTGCTG-3' and 5'-GTAAGCAGAGACCAGAAAGAAGAGTG-3'), *Moxd2* (5'-TGTA CCTTTCTCCCACTCCCTATTGTC-3' and 5'-CCCATGCAACTGGAGATGTTAATTCTG-3'), *Olfr309* (5'-TACAATGGCCTATGACCGC TATGTG-3' and 5'-TCCTGACTGCATCTCTTTGTTCTG-3'), *Olfr727* (5'-CGCTATGTTGCAATATGCAAGCCTC-3' and 5'-GCTTTGA CATTGCTGCTTTACCTC-3'), and *Olfr618* (5'-CATGAACCAATGTACCTTTTCCTCTC-3' and 5'-AAACCTGTCTTGAATTTGCTTTG TC-3'). The PCR products were cloned into pGEM-T Easy vector and the probes were obtained by *in vitro* transcription of the plasmids, using SP6 or T7 RNA Polymerases (Roche) and DIG RNA Labeling mix (Roche).

QUANTIFICATION AND STATISTICAL ANALYSIS

Information on gene expression thresholds for spatial differential expression analysis is described in the method details section. The presence of a spatial signal along the 3 axes was verified via the Moran's I statistic (see relevant section above). The presence of

spatial non-random patterns was tested using the Ljung-Box test and the resulting p values were adjusted using the FDR method (see relevant section above). Consistency between different datasets and replicates, as well as association between independent data were tested using Spearman correlation tests. Mann-Whitney U tests were employed to test the statistical significance of differences between two distributions. Finally, a cross validation test was used to quantify the accuracy of our Random Forests model through the root mean square error (RMSE). Statistical tests were performed using R (version 4.1.2). Statistical details are reported in the Main text, Figures and Figure legends, the [STAR methods](#) section and [supplementary tables](#). N represents the number of biological replicates (animals) we analyzed. Boxplots are centered at the median of the distribution, the bottom and top of the box represent the 1st and 3rd quartiles respectively, and the whiskers extend for an additional 1.5 times the interquartile range.

Supplemental information

**A 3D transcriptomics atlas of the mouse nose
sheds light on the anatomical logic of smell**

Mayra L. Ruiz Tejada Segura, Eman Abou Moussa, Elisa Garabello, Thiago S. Nakahara, Melanie Makhoulouf, Lisa S. Mathew, Li Wang, Filippo Valle, Susie S.Y. Huang, Joel D. Mainland, Michele Caselle, Matteo Osella, Stephan Lorenz, Johannes Reisert, Darren W. Logan, Bettina Malnic, Antonio Scialdone, and Luis R. Saraiva

SUPPLEMENTAL FIGURES

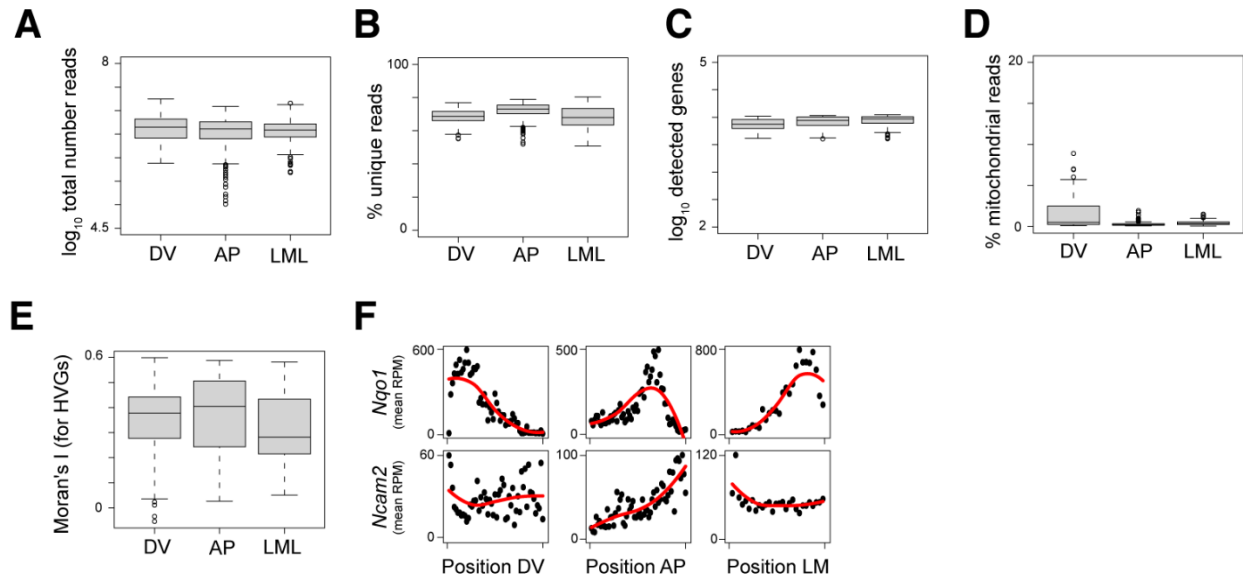


Figure S1. TOMO-seq data QC, Related to Figure 1 and Table S1. (A) Boxplots showing the distributions of the \log_{10} total number of reads per sample in each axis (DV = dorsal-ventral; AP = anterior – posterior; LML = lateral-mid-lateral). (B) Boxplots of percentage of uniquely mapped reads per sample per axis. (C) Boxplots of distributions of \log_{10} detected genes per sample per axis. (D) Boxplots of percentage of mitochondrial reads per sample per axis. (E) Boxplots showing the distribution of the Moran's I statistics calculated for the top 100 Highly Variable Genes per axis. P-values are computed for each gene and then combined with the Simes' method. The combined p-values are $< 2.2 \times 10^{-16}$ for all axes. (F) Normalized expression of canonical OM spatial marker genes along the three axes. Red line showing fits with local polynomial models.

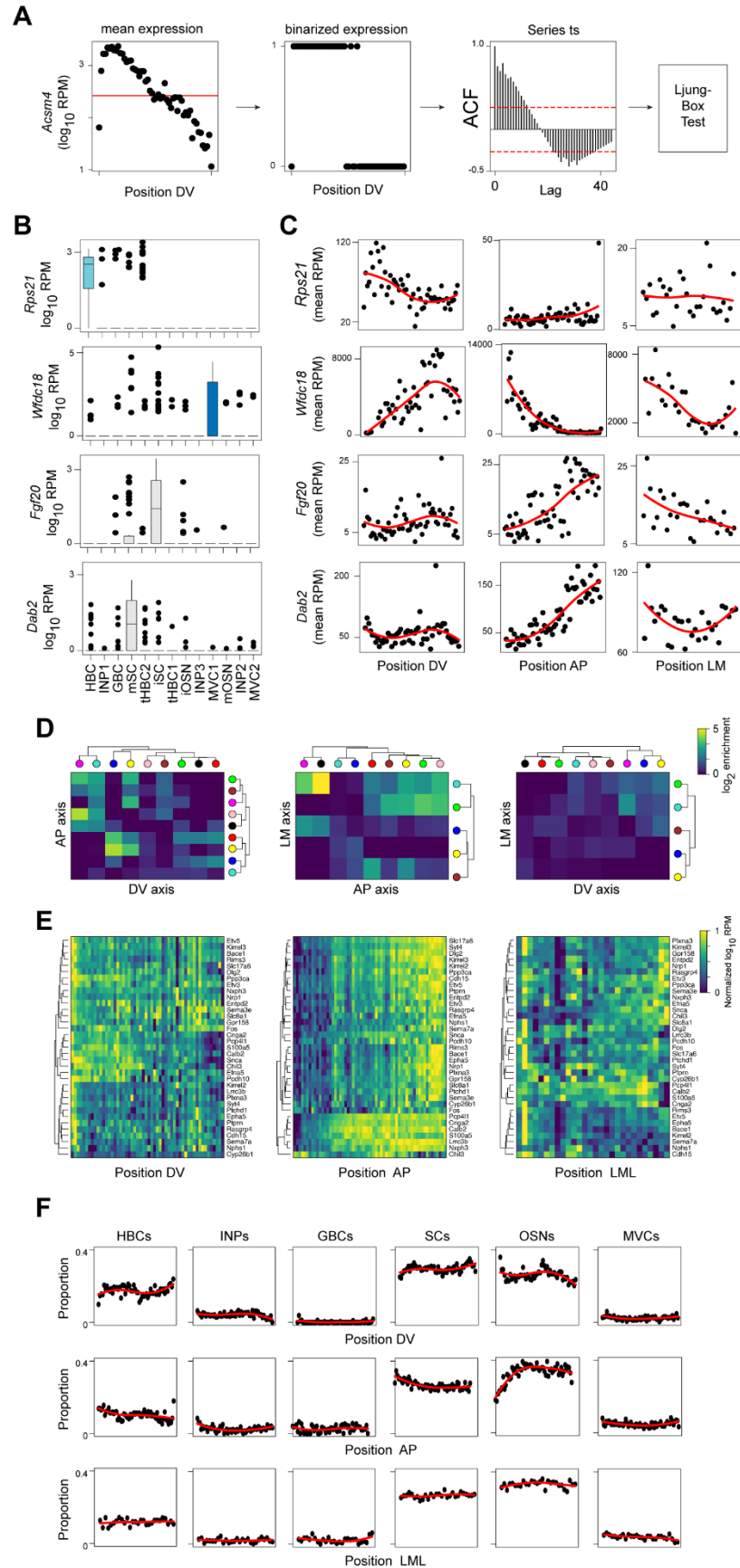


Figure S2. Spatial differential expression analysis, Related to Figure 2 and Table S2. (A) Schematics of strategy to find spatially differentially expressed genes; as an example, data for *Acsn4* along the dorsal-ventral (DV) axis is shown: Gene expression was binarized according to whether the expression per slice was higher or lower than the median expression (red horizontal line). Then, we computed the autocorrelation function for different values of the lags, and we applied the Ljung-Box test to verify whether the autocorrelation values are significantly higher than zero. (B) Box plots of example genes' expression (\log_{10} reads-per-million, RPMs) distributions in different cell types. None of these genes is expressed in mOSNs (INP = Immediate Neuronal Precursors; GBC = Globose Basal Cells; mOSNs = mature Olfactory sensory neurons; iOSNs = immature Olfactory Sensory Neurons; MVC = Microvillous Cells; iSC = Immature Sustentacular Cells; mSC = Mature Sustentacular Cells; HBCs = Horizontal Basal Cells). (C) Spatial gene expression trends along each axis of the example genes shown in panel B. (D) Heatmap showing the \log_2 enrichment for the intersection between different gene clusters (indicated by colored circles) across pairs of axes, after excluding *Olf* genes. (E) Heatmaps showing normalized mean expression of the neuronal activity marker genes listed in Table S2 from (Wang et al., 2017) along the three axes. (F) We used cell type deconvolution analysis to estimate the cell type composition per section along the three axes. The red line marks the fit with local polynomial models.

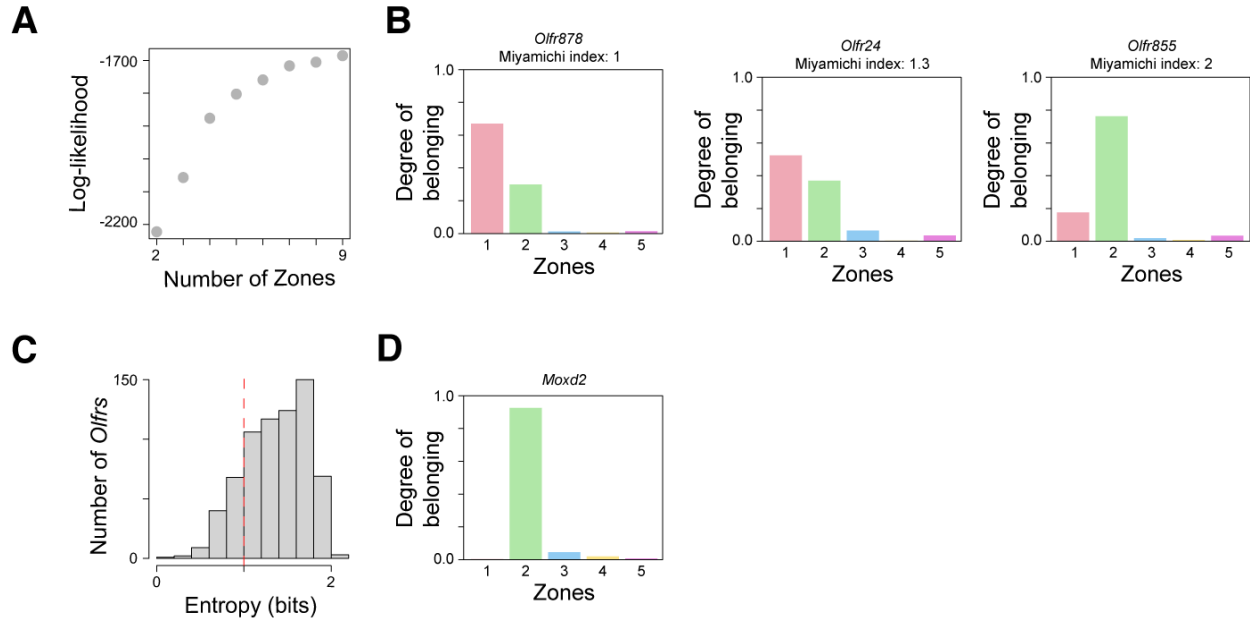


Figure S3. *Olfr* genes 3D zones, Related to Figure 3. (A) Log-likelihood values for fits with LDA models as a function of the number of zones. (B) Bar plot showing the degrees of belonging of *Olfr* genes with overlapping spatial patterns (Miyamichi indexes of 1, 1.3 and 2 respectively). (C) Distribution of entropy values of our 689 spatially differentially expressed *Olfrs*. The *Olfrs* with entropy values less than 1 bit (vertical red line) can be considered to fit mostly in one zone. (D) Bar plot showing the degrees of belonging of *Moxd2*.

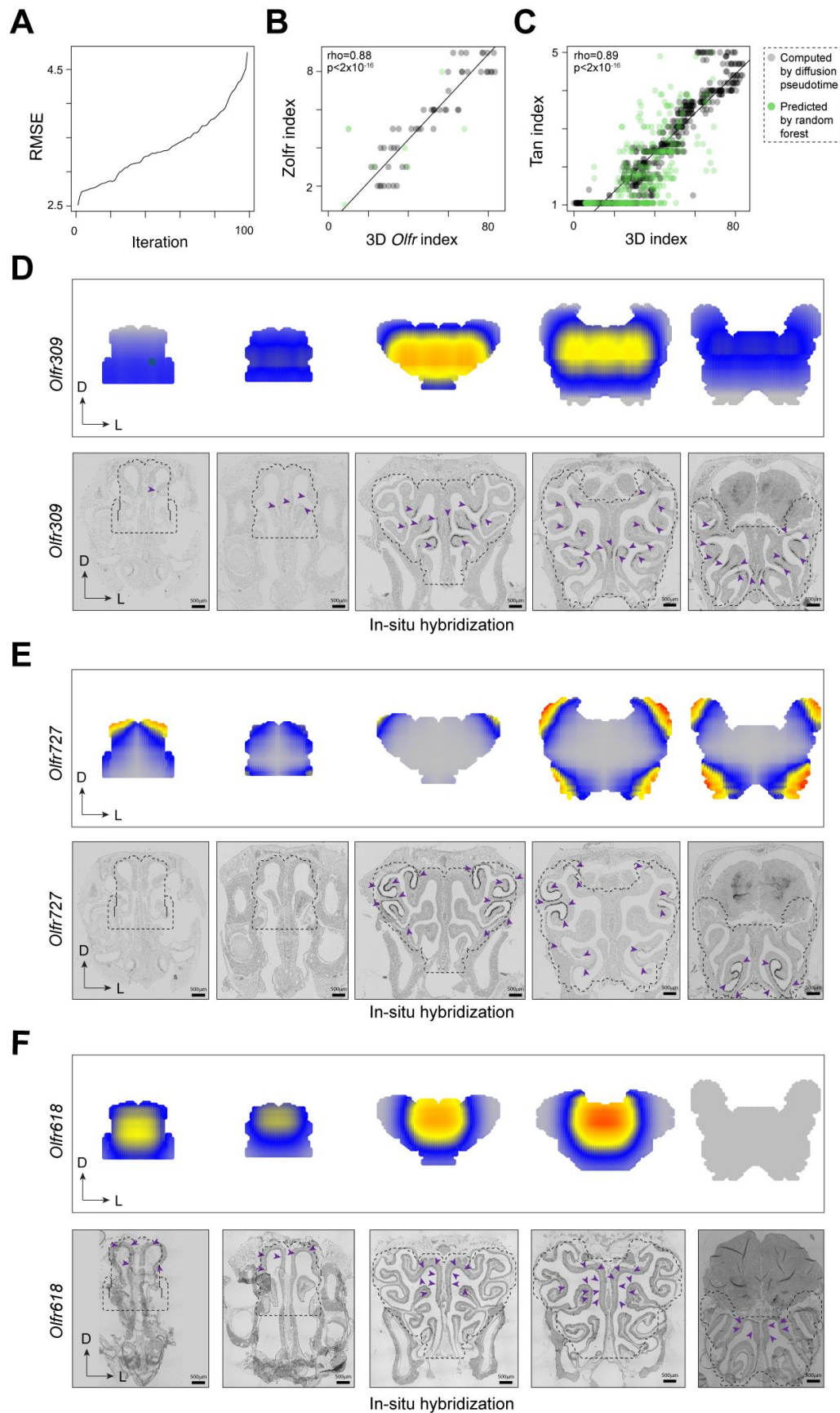


Figure S4. *Olf* 3D index prediction, Related to Figure 4 and Tables S3 and S4. (A) Root mean square error (RMSE) per iteration of the cross-validation test for the Random Forest model used to predict 3D indexes. (B) Scatter plot illustrating the comparison of our 3D indexes versus the “Zolfr indexes” defined by (Zapiec and Mombaerts, 2020) from ISH data. For this comparison, these zones were numbered from 1 to 9 from the most dorsal to the most ventral. Black circles indicate *Olf*s detected in our dataset; green circles are *Olf*s for which indexes were predicted with Random Forest. The correlation coefficients computed separately on these two sets of *Olf*s are respectively $\rho=0.92$, $p\text{-value}<2\times 10^{-16}$ and $\rho=0.44$, $p\text{-value}>0.05$. (C) Scatter plot showing the correlation of our 3D indexes with the “Tan Indexes” estimated by (Tan and Xie, 2018), who performed RNA-seq on 12 samples at different positions along the dorsal-ventral axis of the OM and estimated indexes using as reference the ~80 *Olf*s analyzed in (Miyamichi et al., 2005) via ISH. Black circles indicate *Olf*s detected in our dataset; green circles are *Olf*s for which indexes were predicted with Random Forest. The correlation coefficients computed separately on these two sets of *Olf*s are respectively $\rho=0.95$, $p\text{-value}<2\times 10^{-16}$, and $\rho=0.68$, $p\text{-value}<2\times 10^{-16}$. (D-F) In-situ hybridization experiment validating the predicted 3D spatial expression patterns for *Olf*309 (D), *Olf*727 (E), and *Olf*618 (F). Note that *Olf*618 is expressed in Zone 1, consistent with its predicted spatial expression pattern and calculated 3D index of 7.42 (Figure 4 N, O). Purple arrowheads indicate the location of ISH labeled cells. The dotted outline indicates the borders of the OM dissected and used in the RNA-seq experiments and for the construction of the 3D model.

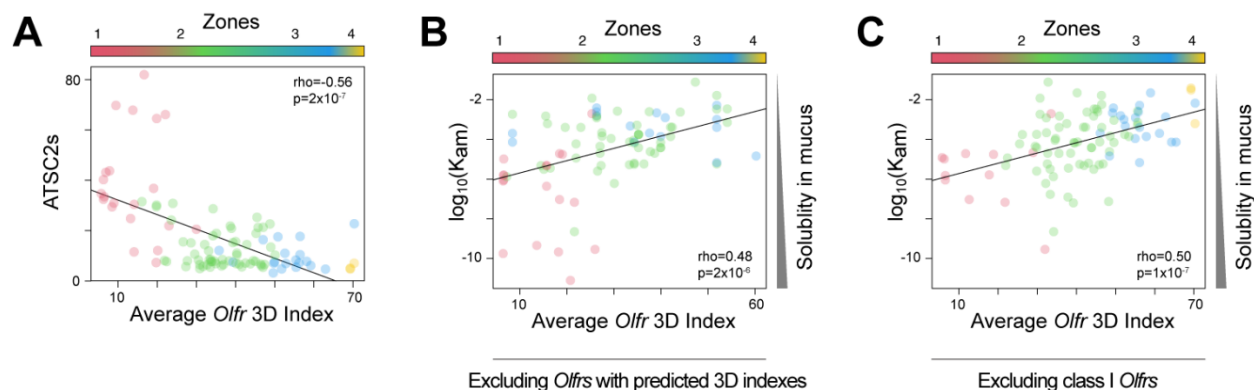


Figure S5. Physiological role of the zones, Related to Figure 6 and Table S6. Scatter plot illustrating the correlation between ATSC2s of the odorants and the average 3D indexes of their cognate Olfrs. Only odorants for which we know at least two cognate Olfrs (110) were used here. Odorants are colored according to the zone they belong to (defined as the zone with the highest average degree of belonging computed over all cognate receptors). (B) Scatter plot illustrating the correlation between air/mucus partition coefficients of the odorants and the average 3D indexes of their cognate Olfrs. Only odorants which are detected by Olfrs present in our TOMO-seq dataset (87) were used here. (C) Scatter plot illustrating the correlation between air/mucus partition coefficients of the odorants and the average 3D indexes of their cognate Olfrs. Only odorants which are detected by Class II Olfrs (101) were used here.